Department of Geology

Earth Sciences Institute

Faculty of Mathematics and Natural Sciences

The Hebrew University of Jerusalem

THE HEBREW UNIVERSITY OF JERUSALEM

Evolution of Normal Faults: Displacement Patterns in 3D Seismic from the Eastern Levant Basin

Thesis for the partial fulfliment of the Degree of Master of Science

Submitted by:

Nadav Navon

Under the supervision of:

Prof. Amotz Agnon

Dr. Benjamin Medvedev

September 2018

אלול תשע"ח

Acknowledgments

I would like to thank my supervisors Amotz Agnon and Benjamin Medvedev for their support and patience at any given moment. For giving me the opportunity to explore my fields of interest. I have learned a lot from their knowledge and experience.

This work would not have been possible without the help of Dr. John Hall, for all the 'Neev Center' facilities I used which allowed this work to come to fruition. For sharing his experience which helped me professionally as well as personally.

I would like to thank Schulumbeger™ for the use of the Petrel E&P Software Suite and to Adira Energy for generously providing the seismic data.

My diligent friends at the 'Neev Center': Osnat Barnea, Yaniv Darvasi, Guy Tzarfati, Ron Algon, Jonathan Keinan and Lior Kamhagi for their support and field adventures. You became a second family to me.

My friends from the geology department: Yevgeny Krayserman, Nicole Behar, Natalie Neagu, Evyatar Cohen, Ilya Kutuzov and Moshe Politi for their support during this work. My friends from the oil rig: Sharon Reuveni, Michal Koren, Nisim Shushan, Gil Arnon, Angelo Bianco and Zoran Veseli for their support and great coffee breaks during the long shifts.

A special thanks to my close friend Leor Oren. His advice always put things in the right perspective.

To my beloved parents Itzik and Mary for always standing by me and for taking pride in my journey. My brothers Asaf, Ariel and Chen, for lifting my up when needed and for their endless support.

Abstract

The continental shelf offshore Israel is densely populated by slump units in the Pliocene -Pleistocene section. The gigantic unit known as the Israel Slump Complex (ISC) and its overburden are incised by thin-skinned fault systems. Quantitative fault displacement analysis presents the relation between the slump units and the evolution of normal faults incising them.

Following structural standard interpretation, slump units and an array of normal faults and are mapped in the Gabriella seismic volume, a high-resolution 3D seismic survey (depth-migrated) located 12 km offshore Netanya. The stratigraphic column of the volume includes the post-Messinian section of Saqiye and Kurkar groups. Fault systems are characterized by unrestricted blind faults and restricted growth faults. The Middle-Late Pleistocene progradational settings make distinguishing the two types of faults a challenge. Fault displacements are analyzed based on ten key horizons using a step-by-step workflow which includes throw-versus-depth profiles, displacement contour diagrams and displacement gradients. Growth stages within the faults are highlighted using expansion indices and restoration models. Combination of these methods proves useful both for growth model classification and accurate fault mapping. Variations in displacement patterns underscore the control of chaotic features, acting to restrict the growing faults.

Two main fault zones are identified: Northern Fault Zone (NFZ) and Southern Fault Zone (SFZ), comprised of N-S and NW-SE striking normal faults, respectively. Four sampled faults yield distinguishable types of growth: (1) Blind fault, where both horizontal and vertical tips close gradually; (2) Restricted growth fault initially evolving as a blind fault, associated with an incision into the ISC at 0.51-0.7Ma; (3) Blind Restricted fault, with two zones of high displacements, associated with the incision of a small slump unit; (4) Blind restricted fault, characterized by high displacement gradients at its deeper part.

We find that chaotic structures control fault activation, which depends on the spatial relation between the structures. This can result either locally with segmented activation within the fault, or with lateral growth initiation on the entire fault. The linkage between proximity to slump units and growth pattern may lie in the compaction potential of the latter.

The research provides empirical evidence for distinguishing a fault growth and blind stages. This can be especially helpful where faults have similar dimensions and ranges of throw values, which result in minor displacement differences. The presented workflow can also be used for illuminating geo-hazards related to fault activation.

Table of Contents

Table of Figures

1. Geological background

1.1 Regional settings

The Levant Basin (Fig. 1) comprises the continental margin that bounds the onshore platform of Israel with the oceanic lithosphere of the eastern Mediterranean Sea (Frey-Martinez et al., 2005). This margin is situated in active tectonic settings, at the zone of interaction between the African, Anatolian, and Arabian plates.

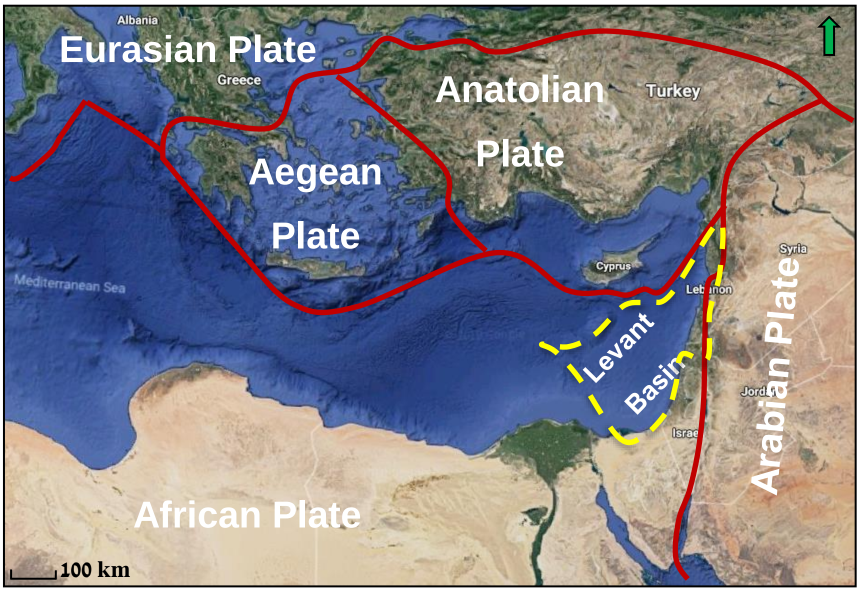

Figure 1. Location map of the Levant Basin and the surrounding plates. Source- Google maps.

The basin evolved from a rifting stage to a convergent stage with respective facies changes dating from Early Mesozoic (Gardosh et al., 2006). The convergent stage, dated to Late Cretaceous and Tertiary, resulted in inversion of structures and in the formation of the Syrian Arc constructional structures and folds (Hensen, 1951; Freund et al., 1975). A major desiccation event in the Mediterranean Sea during the late Miocene, known as the Messinian Salinity Crisis, resulted in the deposition of a thick evaporitic layer, named the "Mavqi'im" Formation (Gvitzman and Buchbinder, 1978). The formation is pinching out laterally against the basin margins as a function of structure and relict topography (Bertoni & Cartwright, 2006). Gradual sea level rise during the post-Messinian succession resulted in renewed sediment transport of the Plio-Pleistocene Yafo Formation (Gardosh et al., 2008). This formation consists of clay-rich marls, sandstones and claystones derived mainly from the Nile Delta (Tibor & Ben-Avraham, 1992).

Tilting of the margin during the Pliocene resulted in two types of gravity-driven deformation: thin-skinned fault systems (Frey-Martinez et al., 2005), and gravitational collapse rooted in the thick Messinian evaporites (Garfunkel & Almagor, 1987;

Cartwright & Jackson, 2008). The gravitational collapse produced a down-dip contraction domain at the basin floor and an up-dip extensional domain at the pinchout of the Messinian evaporites (Bertoni & Cartwright, 2006; Gradmann et al, 2005). Oscillations in the global eustatic sea level and vertical tectonic movements resulted in shoreline advances and retreats (Frey-Martinez et al., 2005). These involved the deposition of interbedded sands, clays and marls on the continental shelf, namely the Hefer Formation (Sivan et al., 1999, Frey-Martinez et al., 2005).

1.2 Israel Slump Complex (ISC)

Frey-Martinez et al. (2006) characterized a major slump complex, named Israel Slump Complex (ISC, Fig. 2), in the late Pliocene succession. The ISC extends almost continuously along the continental margin of Israel, consisting of up to approximately 1000 Km^3 of Pliocene sediments and covering an area of 4500 Km^2, placing it among the world's largest slump deposits (Frey-Martinez et al., 2005). According to Paldor (2016), the ISC is not derived from salt tectonics but from rapid accumulation of unstable sediments slumping westwards.

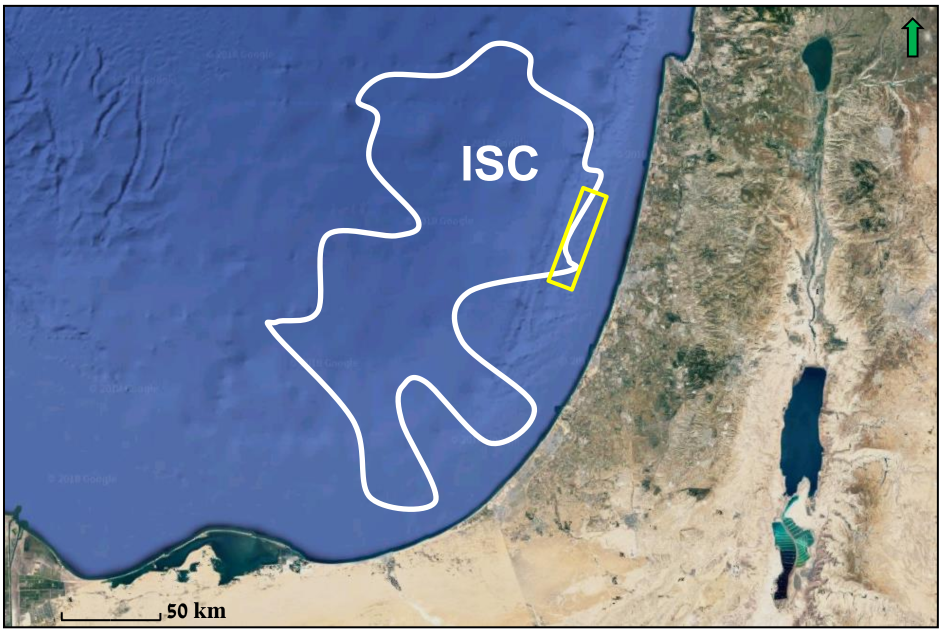

Figure 2. The Israel Slump Complex. The ISC aerial extension (white) with relation to the "Gabriella" 3D seismic data (yellow rectamgle) used in this reseach. Source- Google maps.

1.3 Fault dimensions and displacement terminology

Fault dimensions, i.e. their length and width ,refer to their vertical and lateral extents (Fig. 3a). Displacement refers to the fault's dip-slip component (Fig. 3b), which varies across the fault surface. Displacements are usually highest at the fault surface center and decrease to zero towards the fault tips.

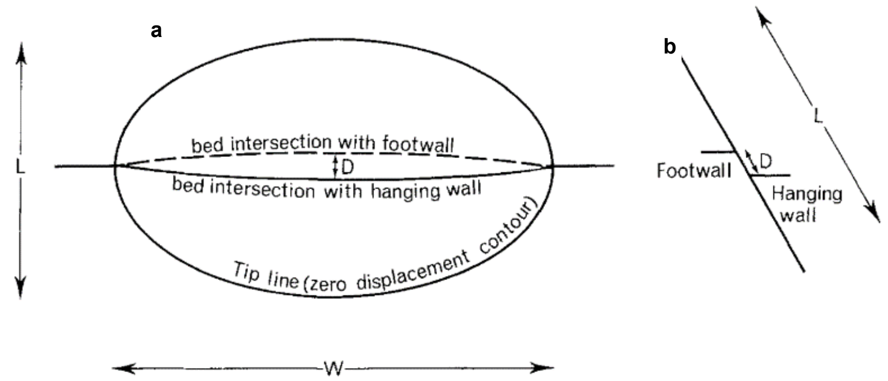

Figure 3. Normal fault displacement geometry. (a) Lateral and vertical extent refers to fault width and length, respectively. D represents dip-slip and it is measured by bed displacement. Fault boundaries are set at zero displacements. (b) Fault displacement viewed in schematic cross section. Modified after Watterson (1986).

1.3.1 Displacement gradients

Displacement gradients are calculated from displacements to the fault tips, where displacements decrease to zero. These can be calculated either in the horizontal or vertical direction. Gradients vary along the horizontal and vertical axes of an ellipse that approximates the perimeter of the fault surface.

Fault displacement geometry is controlled by a dominant ratio:

$\frac{D}{R} =$ Mean Displacement Gradient (Eq. 1)

D = Maximum displacement, $R = \frac{W}{2}$ = Fault surface radius.

Vertical Gradient (VG) is defined as

$\frac{D}{l} =$ VG (Eq. 2)

D = Maximum displacement, l = distance from D to zero displacement. This is measured along the fault strike at equal intervals.

Both horizontal and vertical axes of faults imaged seismically elsewhere with strike dimensions of 1.3-9.7 km show vertical gradients of 0.04-0.22 (Nicol et al., 1996). Displacement gradients are greater in the down dip direction (i.e. vertical gradients) due to mechanical anisotropy (Barnett et al., 1987).

1.3.2 Displacement variations with fault size

The relation between fault maximum displacement (D) and fault width (L) is expressed as:

$D \propto L^{n}$, n ranges between 0.5 - 2 (Cowie & Scholz, 1992; Childs et al., 2017). (Eq. 3)

Cowie & Scholz (1992) state that establishing the fault displacement and length relation is limited due to the variety of fault zone environments. Other studies show that faults from the same systems share similar maximum displacements (Watterson, 1986; Barnett et al., 1987). Watterson (1986) defined n=2, where gradients increase linearly with fault dimensions.

$D \propto L^2 \rightarrow D \propto (2R)^2 \rightarrow \frac{D}{R} \propto 4R$ (Eq. 4)

The relation of D vs. W for numerous fault systems is presented in Fig. 4 (Barnett et al., 1987).

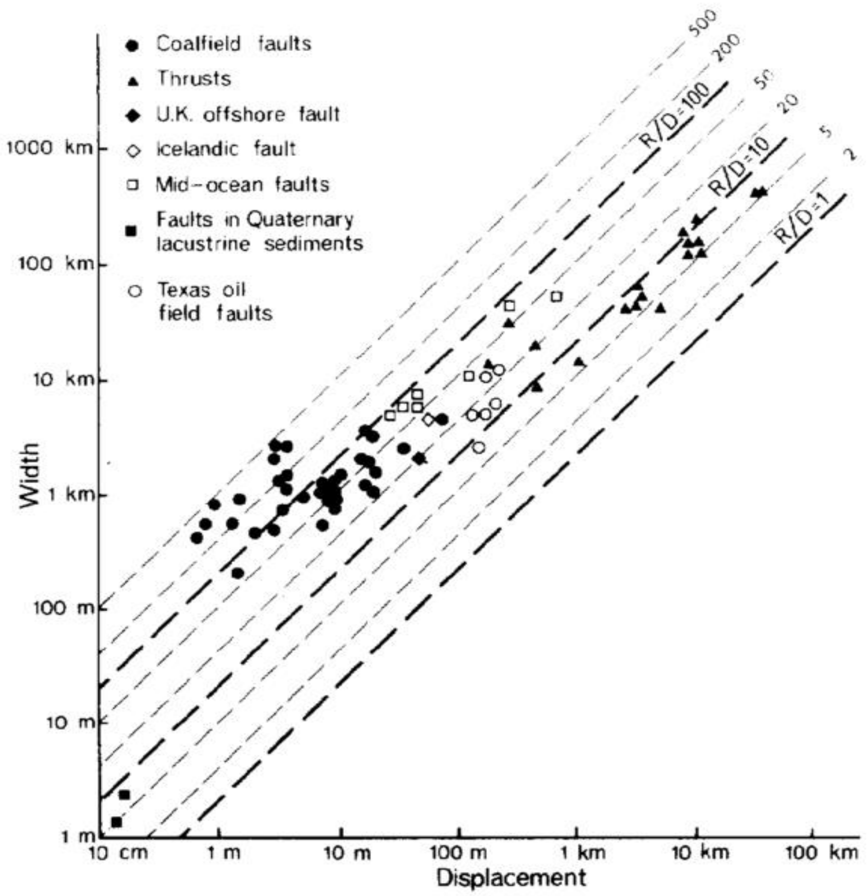

Figure 4. Width versus maximum displacements. The logarithmic plot includes different clusters of normal and thrust faults systems, dashed lines represent the Mean displacement gradient reciprocal. Coalfield faults (Rippon, 1985), Icelandic fault scarps (Laughton and Searle, 1979; Searle, 1983), thrusts (Elliott, 1976), Quaternary faults (Muraoka and Kamata, 1983), Texas oil field faults (Lahee, 1929). Modified after Barnett et al., (1987

1.3.3 Aspect Ratio (AR)

Fault aspect ratio is defined as:

$$A.R = \frac{Fault\ Strike\ dimension}{Fault\ Dip\ dimension} = \frac{2R}{L} = \frac{W}{L} \quad \text{(Eq. 5)}$$

$$A.R > 1 \quad = \quad Horizontal\ elongation$$

$$A.R < 1 \quad = \quad Vertical\ elongation$$

In layered rock systems, often the case for sedimentary basins, the principal control on the shape of post-sedimentary faults is mechanical anisotropy (Nicol et al., 1996). As a result, fault propagation in the dip direction is slower relative to the horizontal direction, resulting in AR > 1.

1.4 Fault classification

1.4.1 Restricted & Unrestricted faults

In a given fault system, many individual faults interact with neighboring faults (Nicol et al., 1996). The likelihood of fault interaction increases with fault system maturity, expressed by the increase in fault size and density (number of faults per unit volume). Because of such interactions, distinguishing between ***unrestricted*** *and* ***restricted*** faults is useful (Fig. 5, Nicol et al., 1996).

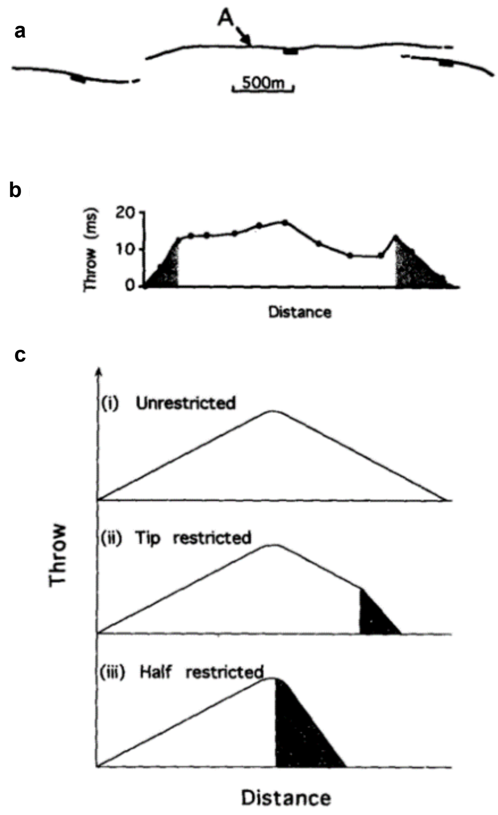

Figure 5. Restricted & Unrestricted faults. (a) Schematic fault map, showing traces of normal faults. (b) Throw values along fault A present an asymmetrical restricted pattern. (c) Schematic models for restricted and unrestricted faults. Black zones represent the restricted parts. Modified after **Nicol et al. (1996).**

Unrestricted faults, also referred to as "blind", are effectively isolated faults. These faults evolution has not been perturbed or intersect with either a free surface or substantial layers or geological bodies, e.g. salt diapirs or neighboring faults. . Unrestricted faults are characterized by uniform displacement gradients in either the horizontal or vertical directions. Restricted fault surfaces are characterized by less regular displacement patterns with a single or no axis of bilateral symmetry (Fig. 5c). Such faults show increased displacement gradients close to the confining feature, e.g. adjacent faults or a free surface. Generally, most faults are considered restricted. Lateral and vertical restricted faults are associated with aspect ratios of < 1.3 and > 2.5, respectively (Nicol et al., 1996).

1.4.2 C-type & M-type faults

Displacements along fault profiles can be plotted as throw vs. depth diagrams, known as T-Z plots (See chapter 2.3.1). These plots can exhibit C-type (cone shaped) and M-type (mesa shaped) profiles (Figure 6) (Muraoka & Kamata, 1983).

C-type profiles, characterized by nearly symmetrical throw profiles, are typical of faults formed in homogeneous materials (Fig. 6a). M-type profiles are characterized by a broad central section with minor displacement variations, abruptly diminishing at the fault tips (Fig. 6b), indicating that the fault cuts through rigid material (Muraoka & Kamata, 1983). Both types are distinguished quantitatively, where the / ratio of the M-type pattern is nearly twice as large of the C-type. Variations of C & M-type profiles across faults can be explained seismic-stratigraphic variations, particularly for displacement patterns controlled by lithological changes. In research offshore Gaza, blind faults showed M-type profiles rather than the expected C-type profiles (Baudon & Cartwright, 2008b).

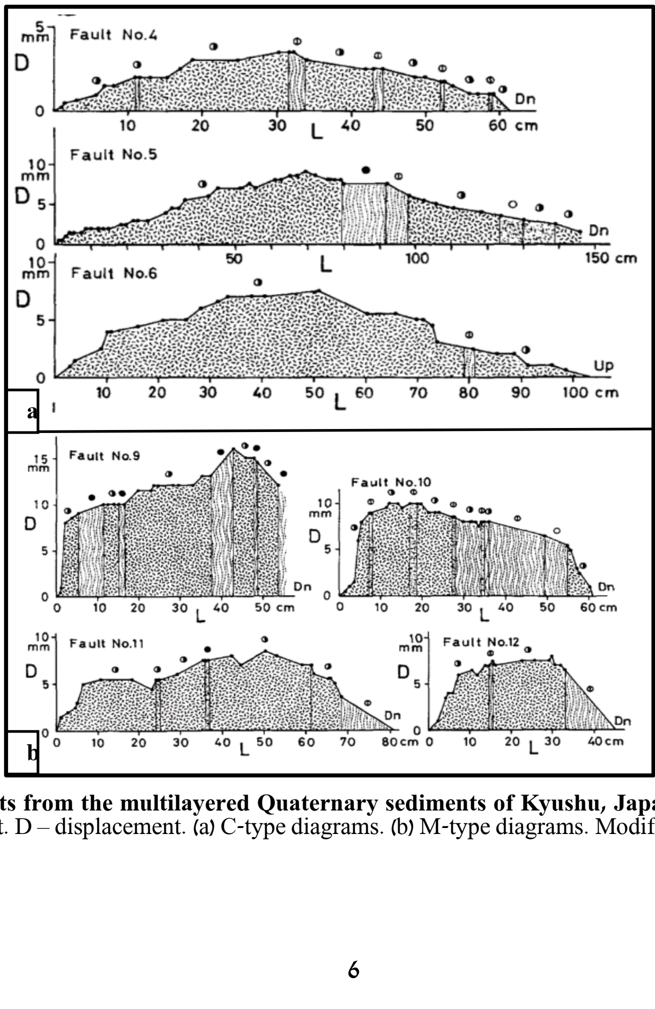

Figure 6. T-Z plots from the multilayered Quaternary sediments of Kyushu, Japan. L referest to the fault vertical extent. D – displacement. (a) C-type diagrams. (b) M-type diagrams. Modified after Muraoka & Kamata (1983.

1.4.3 Growth faults

Growth faults are syn-depositional extensional faults that initiate and evolve parallel to passive margins with high sediment supply (Galloway, 1986; Schlische & Anders, 1996). Most growth faults are synthetic and have long-term continuous displacements. In shelf and upper slope environments, sedimentation rates often keep pace with fault displacement rates (Edwards, 1995; Cartwright et al., 1998). As a result, changes in stratigraphic thickness across growth faults enable one to calculate the throw accumulated during deposition (Edwards, 1995; Baudon & Cartwright, 2008a).

1.5 Fault growth models

Single faults can consist of numerous fault segments (Walsh & Watterson, 1989). Conceptual models for development of these faults are illustrated in Fig. 7 (Child et al. 2017). The models are classified based on two criteria:

Coherent versus Non-coherent- Whether the faults developed as elements within a coherent structure (coherent) or by linkage of mechanically and kinematicaly isolated segments (non-coherent).

Constant length versus Propagating - Whether faults initially reach their total length with low displacement values (constant-length), or during the process of displacement (propagating).

Higher sampling rate and shorter trace spacing results in higher horizontal resolution. In 2D/3D seismic data, resolution depends upon the data bin size - inline and crossline spacing (Fig. 10b).

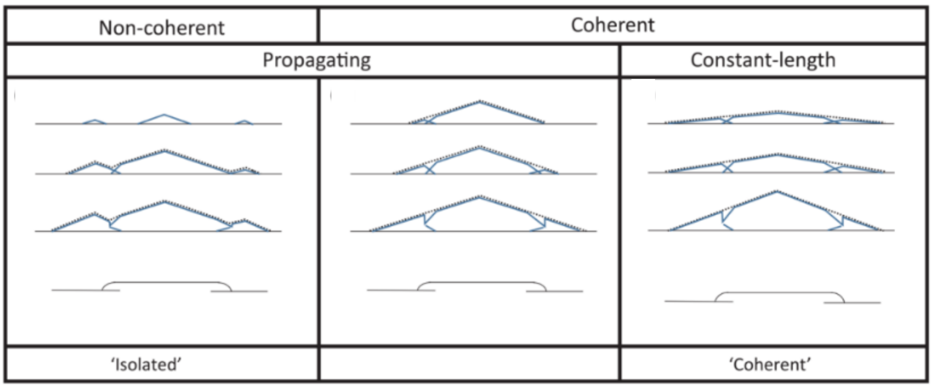

Figure 7. Conceptual models for growth of a single fault consisting of numerous faults. The models result in the same map views. Solid lines- displacement values for each segment. Dashed lines- profiles of aggregate displacements. Modified after Childs et al. (2017).

2. Methods

2.1 Reflection seismology

Reflection seismology is a method used to create an image of the subsurface based on the principles of wave propagation. Using this method, a man-made energy source (hammer, dynamite, air gun, etc.) generates waves which propagate in the subsurface and are reflected back from contacts between rocks with different physical properties. These reflections, refered as reflectors in seismic data, are also addressed as seismic response or seismic events (Herron, 2011). The waves arrival times are received at the surface by geophones or hydrophones and recorded.

The waves intensities and velocities are controlled by the physical properties of the bedrock and referred to as acoustic impedance (AI):

$AI = V\rho$ (Eq. 6)

$V -$ Compressional wave velocity $[\frac{m}{s}]$

$\rho -$ Bulk density $[\frac{kg}{m^3}]$

AI difference between two layers is required for a wave to reflect from their contact. This difference is, calculated as Reflection Coefficient (RC):

$RC = \frac{AI_1 - AI_2}{AI_1 + AI_2}$ (Eq. 7)

Travel times of waves, from source generation to the receivers after reflecting from AI boundaries, are known as the two-way travel time (TWTT). This is than processed into 'seismic data', which represents a composite response to many closely spaced impedance boundaries (Herron, 2011). The time-based seismic data can be converted to depth-based data by reprocessing using velocity models and check-shot data. Lithological boundaries are displayed as reflectors, or *horizons*. Amplitude associated with a particular reflector is proportional to the RC value, where the sign of RC controls the polarity of the arrival at the receiver (Fig. 8).

2.1.1 Seismic resolution

Resolution is the ability to distinguish between objects. Seismic resolution defines how large an object needs to be in order to be visible in the seismic data. Resolution depends upon wavelength, wave frequency and seismic velocity, where:

$\lambda = \frac{V}{f}$ (Eq. 8)

$\lambda - Wavelength\ [m]$

$V - Seismic\ velocity\ [\frac{m}{s}]$

$f - dominant\ frequency\ [hz]$

Seismic velocities, in the context of hydrocarbon exploration, in the subsurface range between 2000-5000 $\left[\frac{m}{s}\right]$, generally increasing with depth. Dominant frequencies range between 20-50 $[Hz]$ and decrease with depth as higher frequency waves attenuate (Yilmaz, 2010). This results in higher and lower resolution at shallow depths, respectively. This limits the ability to identify fault displacements at greater depth. Multiple reflections from shallow depth can appear as separate events, thus limiting seismic resolution as well. Data acquisition settings such as sampling rates (the number of measurements per second) and trace-spacing (the distance between subsurface sampling points (Veeken & Moerkerken, 2013), which equals half of receiver spacing) also control seismic resolution.

Vertical and horizontal resolution

Seismic resolution is typically different for two planes: vertical versus horizontal. In seismic image, an object can be detected if it's larger than either the vertical or the horizontal resolution.

$Vertical\ Reolution = \frac{\lambda}{4},\ \lambda - dominant\ wavelength$ (Eq. 9)

Vertical resolution (Fig. 8) defines how thick a bed must be to allow distinguishable reflections from its top and bottom interfaces with other layers. Hence, two reflective layers must be thicker than ¼ wavelength in orderto be seen separately in the seismic data.

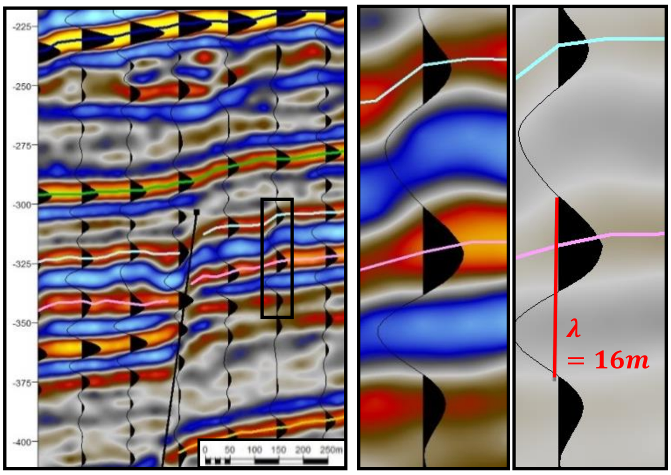

Figure 8. Vertical resolution in depth-based seismic data. Left- a typical cross section. Red and blue reflections represent positive and negative RC. Right- Dominant wave length of 16m results in 4m vertical resolution in this particular section of the seismic data.

Higher sampling rate and shorter trace spacing results in higher horizontal resolution. In 2D/3D seismic data, resolution depends upon the data bin size - inline and crossline spacing (Fig. 10b). Horizontal resolution is controlled by the trace spacing and therefore by the distance between subsurface sampling points (Veeken & Moerkerken, 2013). In 2D/3D seismic data, resolution depends upon the data bin size - inline and crossline spacing (Fig. 10b).

2.1.2 Seismic interpretation

Seismic interpretation is defined as the art of inferring the geology from seismic data. This includes the interpretation of geological structures related to sequence stratigraphy, salt structures, faults, folds, etc. . Seismic interpretation in 3D has proven an excellent means for delineating internal structure and regional extent of slump complexes and fault zones. This method includes the mapping of horizons, faults, and other geological features from the given seismic data (See chapter 2.5). Fault analysis using seismic data presents a challenge due to numerous factors, such as data type, processing techniques, availability of geophysical logs and borehole lithology, and more. In addition, human bias often results in different interpretations as part of the "conceptual uncertainty" inherent in seismic interpretation (Gibbs et al., 2007).

2.1.3 Seismic attributes

A seismic attribute is a quantity extracted from seismic data and analyzed to enhance subtle information in a traditional seismic image (Jibrin, 2009). Seismic attributes can improve seismic interpretation by indicating changes in a waveform as it encounters geological interfaces (Fig. 9). These changes reflect the response of subsurface rocks due to their variable mechanical properties. Seismic attributes can be grouped into two types: physical and geometric. Physical attributes, such as Amplitude, Phase and Frequency, relate to the lithology of the subsurface (Jibrin, 2009). Geometric attributes, such as Variance, Chaos and Dip Illumination, enhance the visibility of the geometrical characteristics (Ngeri, Tamunobereton-ari and Amakiri, 2015). In the current study we used the following geometric attributes to highlight faults:

Curvature - a measure of how deformed a surface is at a particular point. A deformed surface will result in a larger curvature (Chopra & Marfurt, 2007), meaning that this attribute is particularly sensitive to flexures and faults (Fig. 9b). For ideally planar surfaces the curvature value is zero. Volumetric curvature attributes can also provide information on fracture orientation in zones where seismic horizons are not trackable (Chopra & Marfut, 2007).

Variance (edge method) – used for isolating the horizontal discontinuities of amplitudes by producing interpretable lateral changes in acoustic impedance. This attribute produces the same response for the same seismic signature; therefore lateral changes caused by faults are highlighted (Fig 8). Several factors control the variance attributes such as lateral spacing and dip correction, emphasizing discontinuities in these particular orientations (Fig. 9c).

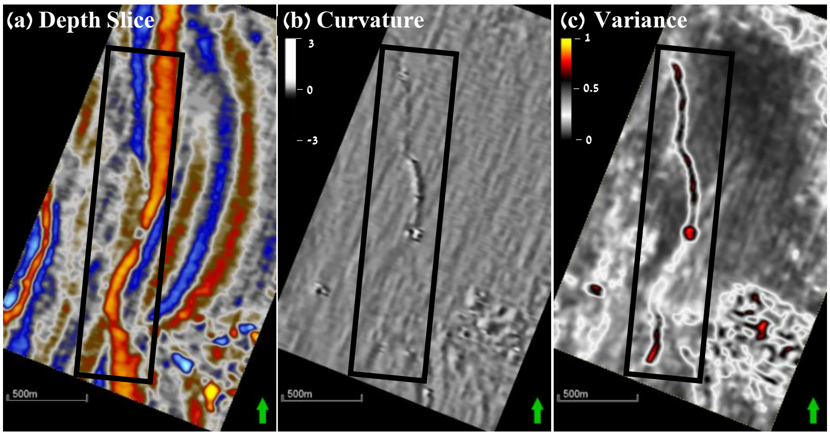

Figure 9. Fault interpretation using seismic attributes. (a) Depth slice of raw data at -464m. (b) Mean curvature attribute highlighting areas of high curvature. (c) Variance attribute presents the fault's boundaries.

2.2 Database

The main dataset for this research is the "Gabriella" pre-stack depth-migrated 3D seismic survey. Located offshore Netanya (Fig. 10a), the survey covers an area of 525 km^2 with $25X12.5m$ grid spacing (Fig. 10b). The stratigraphic column of the survey includes the post-Messinian section of the Saqiye and Kurkar Groups (Fig. 10c). The Mavqi'im Formation, indicated by high amplitude reflectors, is set between 1000-1400m depth. The lower section of the Yafo Formation, addressed here as the Lower Yafo Formation (LYF), separates the Mavqi'im from the upper Plio-Pleistocene sequences which consist of the Mid-Upper Yafo and Hefer Formations.

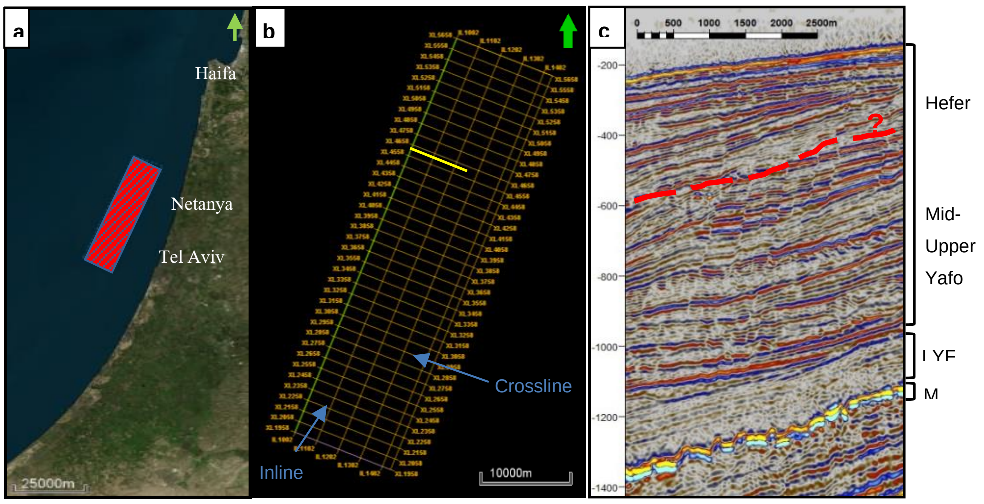

Figure 10. "Gabriella" database. (a) Location map (red rectangle). (b) The seismic data inlines and crosslines grid. (c) Crossline 4585 western part (yellow line in b). Unknown boundary of Yafo and Hefer Formations (thick red dashed line). M- "Mavqi'im" Formation, vertical axis represent depth below sea level (meters).

For displacement purposes, the survey is divided into upper and lower sections, characterized by different vertical resolutions. The upper section, between 200-800m depth, is characterized by shorter wavelength reflections with 4m vertical resolution. The lower section, between 800-1200m depth, is generally characterized by longer wavelengths with 8m vertical resolution.

2.3 Fault displacement analysis

Displacement analysis allows recapturing the fault evolution based upon the displacement distribution along its surface. This method was originally constrained by field observations, which allowed limited displacement measurements of exposed faults (Rippon, 1985; Watterson, 1986). Only later, 3D seismic was introduced providing a full spatial perspective (Mansfield & Cartwright, 1996; Petersen, Clausen, & Korstgård, 1992).

2.3.1 Throw vs. Depth plots (T-Z plots)

Displacement analysis using 3D seismic data is practical where a fault intersects continuous reflectors allowing measurement of their displacements. Seismic profiles orthogonal to the fault strike allow displacement measurments., which are then plotted versus the measured depth of the reflections over the hanging wall (Fig. 11). Equal interval cross sections are used in order to obtain displacement variations along the fault surface .

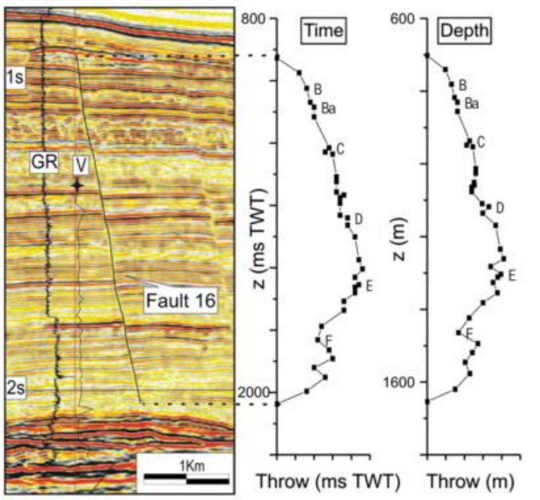

Figure 11. T-Z plot example. A normal fault offshore Gaza with Gamma Ray (GR) and Velocity profiles. Throw vs. time and depth following a depth- conversion using check-shots. Modified after Baudon and Cartwright (2008a).

2.3.2 Displacement Contour Diagram (DCD)

DCDs provide a graphical technique by which displacement values are contoured over a fault plane projection (Barnett et al., 1987); they are also referred to as throw strike-projections. These plots are usually enclosed by a zero displacement contour which sets the fault limits (Fig. 12). Fault evolution is controlled by regional/local settings, such as material anisotropy or intersections with adjacent structures, and therefore can exhibit different DCD patterns.

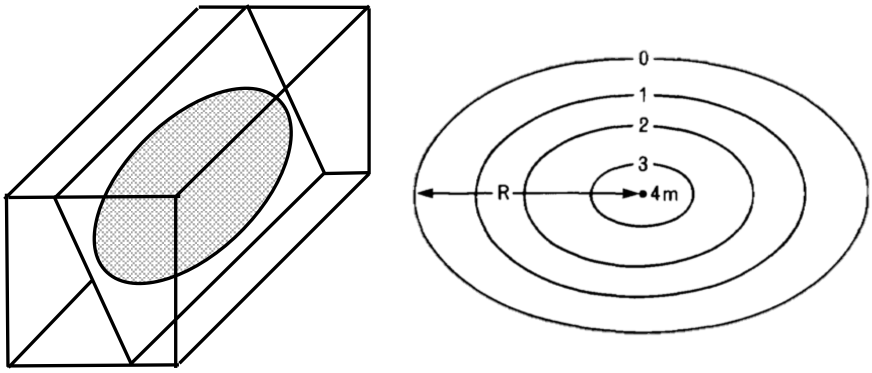

Figure 12. Schematic DCD for unrestricted faults. The example shows maximum displacement of 4m at the fault's nucleation point, decreasing to the tip line 0 contour marking the fault limits. Modified after Walsh and Watterson (1990).

Ambiguity of fault interpretation & DCD solution

Although fault orientations are crucial for the integrity of seismic interpretation, fault mapping using seismic data is considered to be comparatively subjective (Fig. 13a). Freeman (1990) presents an example of different fault interpretations, demonstrating how DCDs allow the interpreter to identify irregularities in the mapping of the original horizons (Fig. 13b).

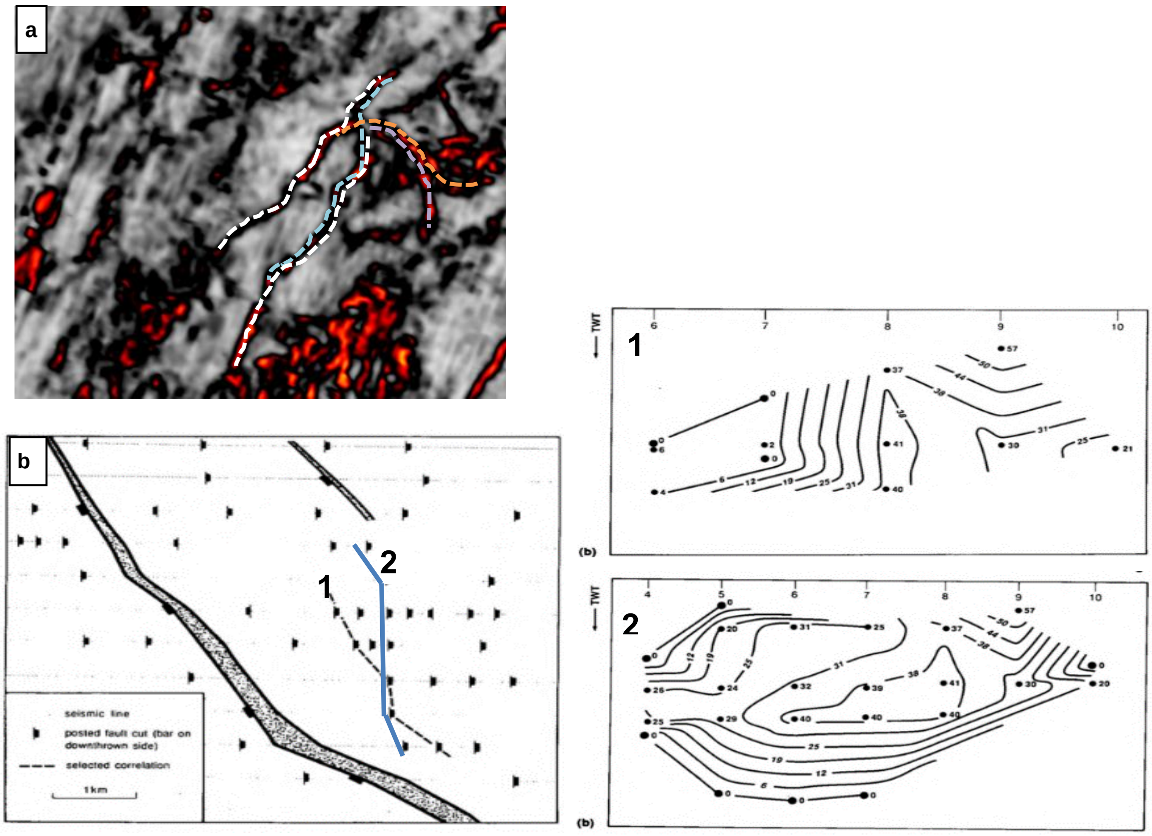

Figure 13. Fault mapping using DCD. (a) Variance depth slice at -446m from the Gabriella dataset. Dashed lines illustrate possible fault interpretations. (b) Cartoon illustrating different fault mapping using seismic data (map view). Fauthl interpretaion 1 presents an irregular displacement pattern, indicative of false interpretation. Fault interpretation 2 resulted with a more elliptical, admissible pattern. Modified after Freeman et al., (1990).

2.3.3 Restoration models

Restoration is a method used for validating fault interpretation, and also assessing whether or not faults had growth phases. Appling this method on seismic data, reflectors are mapped and then sequentially flattened (restored). Each flattening removes the displacement of the restored reflector. This procedure assumes that rock volume does not change due to deformation. Change in displacement of each reflector, other than the one flatted, is examined after each restoration. The method provides quality control of the seismic interpretation. It also can reinforce syn-sedimentary interpretations arising from DCDs.

Under the same geological settings, restorations of isolated and growth faults will show different results. For blind faults, restoration of a nucleation zone is expected to occur at the fault center. In comparison, restoration of the maximum displacement reflector in syn-sedimentary faults is expected at the point of growth initiation at a shallower part of the restoration model. Restoration of syn-sedimentary faults is also expected to exhibit an overlap of reflectors from the hanging wall over the foot wall in growth strata due to higher sediment accumulation.

2.3.4 Expansion Index (EI)

Thorsen (1963) defined a measure of growth strata using expansion index (EI):

$$\frac{\boldsymbol{Thickness\ Downthrown}}{\boldsymbol{Thickness\ Upthrown}} = \boldsymbol{Expansion\ Index} \quad \text{(Eq. 10)}$$

Where:
Thickness downthrown- Thickness of hanging wall unit.

Thickness upthrown- Thickness of foot wall unit.

Assuming constant sedimentation rate, EI indices allow separating faults into different activation phases, where units of higher thickness in the hanging wall are directly related to growth periods. Generally:

- EI =1, no fault activity.
- EI > 1, fault activity.
- Maximum EI values indicate the most significant growth stage.

However, small syn-sedimentry faults with low EI are harder to recognize as they can have low EI values similar to those caused by blind propagation (Baudon & Cartwright, 2008a(?); Childs et al., 2002).

2.4 Fault displacement patterns

2.4.1 The Isolated model

The isolated model refers to unrestricted faults, in which displacements decrease linearly from a maximum at the fault center to zero at the fault tips (Rippon, 1985), solely derived from the fault's propagation gradient (Walsh & Watterson, 1987; Baudon et al., 2008b). DCDs of such faults are expected to form concentric ellipses centered on the point of maximum displacement (Fig. 14a). Numerous studies have described systematic fault displacement distributions considered consistent with this model (Rippon 1985; Chapman & Maneilly 1990; Baudon & Cartwright, 2008b).

2.4.2 Restricted and syn-sedimentary fault models

Restricted faults, either due to growth or neighboring structures, are characterized by increased displacement gradient towards the restricted margin. This results in reduced DCD curvature placing maximum displacement closer to the restricted area (Barnett et al., 1987). According to Barnett et al., (1987) a fault transitioning from blind to growth during its evolution is likely to show maximum displacement at the initial free surface. Restricted faults can also exhibit systematic displacement profiles, yet they show less symmetry in their displacement patterns, making the DCD method useful for separating them from blind faults (Barnett et al., 1987).

Thorsen (1963) stated that for syn-sedimentary faults, decreasing upwards displacement includes blind propagation before reaching the surface. In the growth stage however, decreasing displacements also account for the expansion of sedimentary layers (Baudon et al., 2008b). DCDs of syn-sedimentary faults typically show an abrupt change from sub-horizontal to sub-vertical contours at the syn-fault initiation zone (Fig. 14d, Childs et al., 2002). The sub-horizontal throw contours are an indicator of syn-sedimentary faulting even where growth indices (G.I) are low (Childs et al., 2002).

The boundary between pre- and syn- fault sequences can be derived from the DCD inflection points (Fig. 14d). Stepped T-Z profiles also indicate growth phases, where intervals of zero displacement gradient are interpreted as periods of inactivity, and intervals with positive gradients are interpreted as periods of active growth faulting (Cartwright et al., 1998). Small syn-sedimentary faults can be difficult to distinguish from blind faults, as the overall distribution of displacement of both can be identical (Baudon & Cartwright, 2008b).

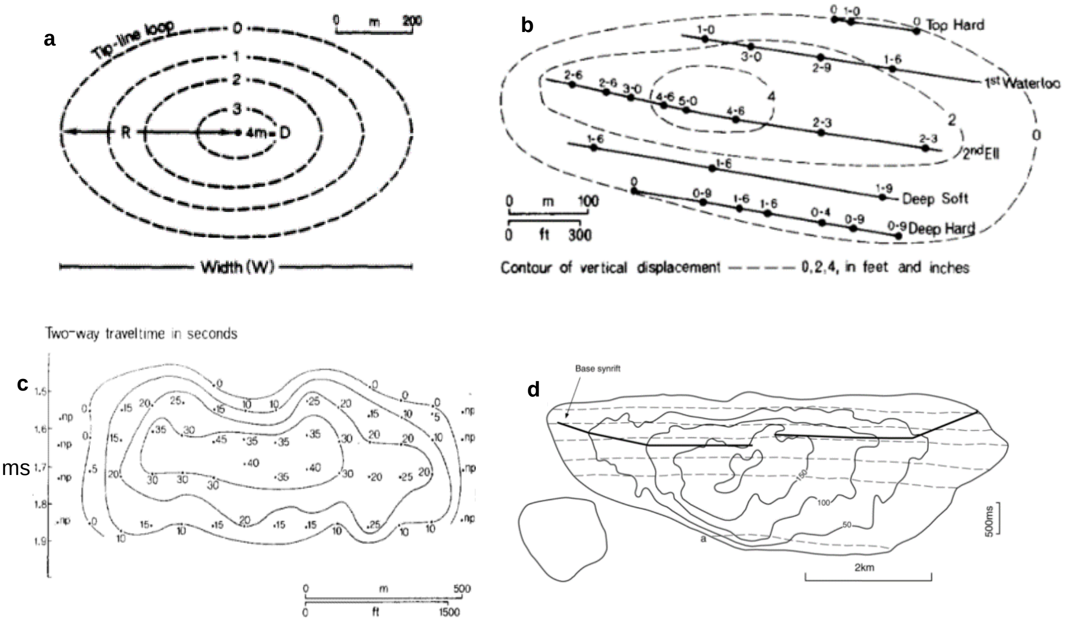

Figure 14. Blind and growth DCD patterns. (a) Schematic diagram of an ideal, blind isolated model. The fault is bounded by a zero displacement contour and shows maximum displacement in the center (Walsh & Watterson, 1990). (b) Displacement contour diagram from a coalfield fault. (c) Displacement contour diagram for a fault from the UK North Sea on a time scale (Barnett, 1987). (d) DCD of a syn-sedimentary fault from the Gulf of Mexico. Transition from blind to growth is marked by black lines crossing the contours' inflection points. Closely spaced contours observed within the syn-fault sequence (Modified after Childs et al., 2002).

2.5 Data workflow and procedure

The research presents a step-by-step protocol for fault displacement analysis.

1. **Seismic Interpretation** - Predominant structures, e.g. fault systems, chaotic zones, and stratigraphic settings are first interpreted by scanning the seismic data. These features are highlighted by seismic attributes to aid interpretation. This is followed by mapping of ten key horizons, produced by impedance differences thus represent different layers in the seismic data. The horizons, identified on both sides of the fault, allow to measure vertical displacements of the layers. Areas where reflections are observed can imply slump structures. Continuous reflections above and below faults indicate unfaulted layers, yet this is limited to seismic resolution especially at greater depth. These allow to measure the faults displacement and define their vertical boundaries. Faults are mapped manually using closely-spaced cross sections, and validated combining seismic attributes analysis.
2. **Displacement measurements-** Displacements are measured at closely-spaced intervals of 62.5 meters using cross sections orthogonal to the strike of the faults. Offsets are measured for all key horizons and for some additional reflectors between them (Fig. 15a) and are tabulated.

3. **T-Z plots-** Displacements are plotted on T-Z plots (Fig. 15b), where T represents the measured displacement and Z represents horizon depth, conventially referring to the hanging wall. The plots show the displacement patterns along fault length in each crossline.

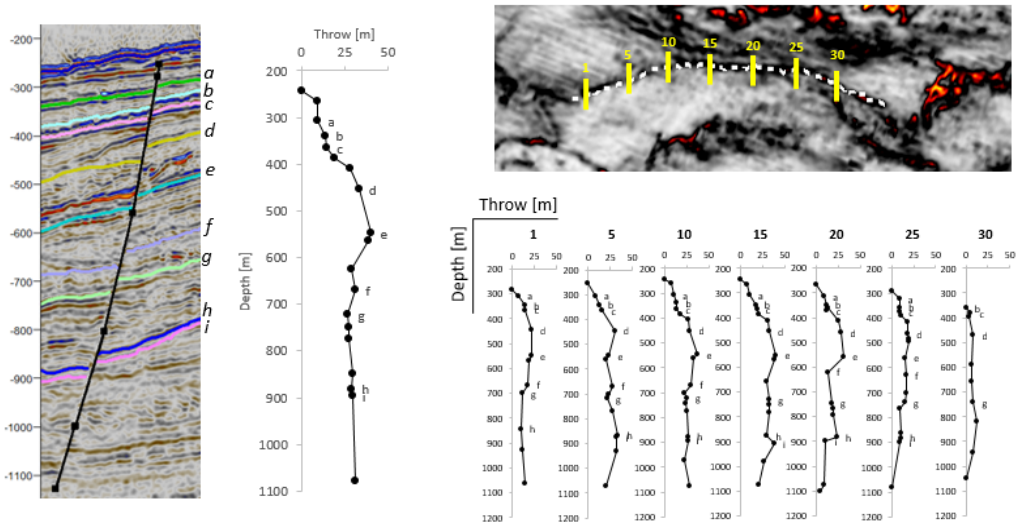

Figure 15. Displacement measurements procedure. (left) Seismic cross section illustrating key horizons mapped, and plotted displacement measurements. (right) Top: Variance depth slice with seven crosslines . Bottom: The crosslines T-Z plots demonstrating displacement variations along the fault.

4. **DCD-** Displacement measurements are arranged in an X, Y, Z table for each fault, where X, Y and Z represent the distance along the fault surface, displacement depth on the hanging wall, and displacement values, respectively. Results are plotted using kriging interpolation with Surfer 2015 by Golden Software.
5. **Restoration-** Key horizons are divided into seismic packages (16a). Each horizon is then flattened (restored) in order to detect younger growth phases. This is indicated by where seismic packages from the hanging wall overlay their corresponding footwall packages, above the restored horizon. This procedure is carried out on three crosslines in each fault, representing Northern, Center and Southern domains. These restoration models are also used in order to detect thickness variations along the fault surface. The faults are restored using the Petrel restoration module.
6. **EI values-** The thickness of each seismic package is measured on each side of the fault for their EI values. These are calculated for all seismic packages and used as input for growth fault detection (Fig. 16b).

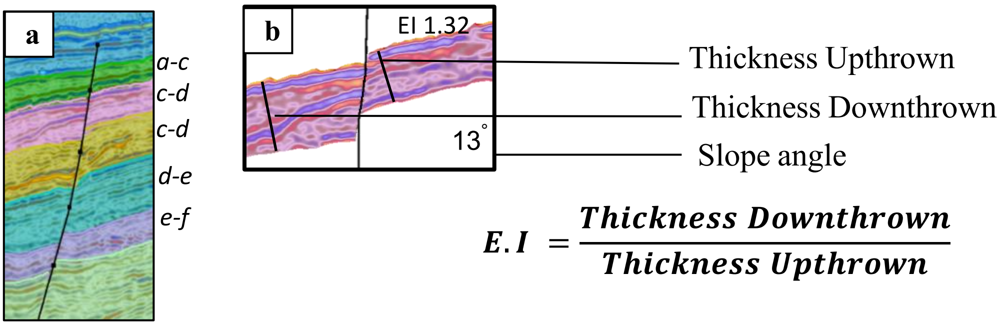

$$E.I = \frac{Thickness\ Downthrown}{Thickness\ Upthrown}$$

Figure 16. Seismic packages separation for restoration purposes, followed by EI calculations. Packages are divided between selected key horizons and then measured separately for their EI values.

3. Research goals

The research goal is to analyze the evolution and propagation history of selected normal faults based on quantitative displacement analysis, and explore the interactions between fault displacement patterns and the chaotic structures incised by them.

Numerous studies focused on basin development and fault analysis in the Eastern Levant basin mainly used time-based seismic data (Garfunkel, 1984; Frey-Martinez et al., 2005; Baudon & Cartwright 2008a,b). We investigate faults development based on depth-calibrated 3D seismic data, which allows quantifying vertical displacements without the uncertainty of time domain data.

Objectives:

1. Produce detailed T-Z and DCD plots for numerous faults in the "Gabriella" survey.
2. Compare displacement patterns of the faults incising chaotic features with other faults, both restricted and unrestricted.
3. Calculate EI values and examine restoration models to gain insights regarding fault evolution.

4. Results

4.1 Seismic interpretation

The "Gabriella" seismic data is characterized by numerous chaotic features interpreted as slump structures. Some of these features appear as weak reflections and others as isolated chaotic bodies. Most notable is the Chaotic Zone (CZ) in the SW region of the survey, (Fig. 17a), previously interpreted as one of the Israel Slump Complex (ISC) head scarps (Paldor, 2015; Eruteya et al., 2016; Safadi et al., 2017). The CZ lays ~200m above the Mavqi'im Formation. Its dimensions within the survey area are 12 km in length and over 500m in thickness at its southern part, thinning to about 100m thickness in its northern part. Another notable structure is a NW-SE large channel situated next to the CZ at the Mavqi'im Formation top and incises a NE-SW anticline. According to Paldor (2015), folding of the Mavqi'im Formation preceded the channel incision. The LYF fills the bottom part of the channel, and is overlain by semi-chaotic reflections forming a lens-shaped structure, hereafter semi-chaotic lens(Fig. 20).

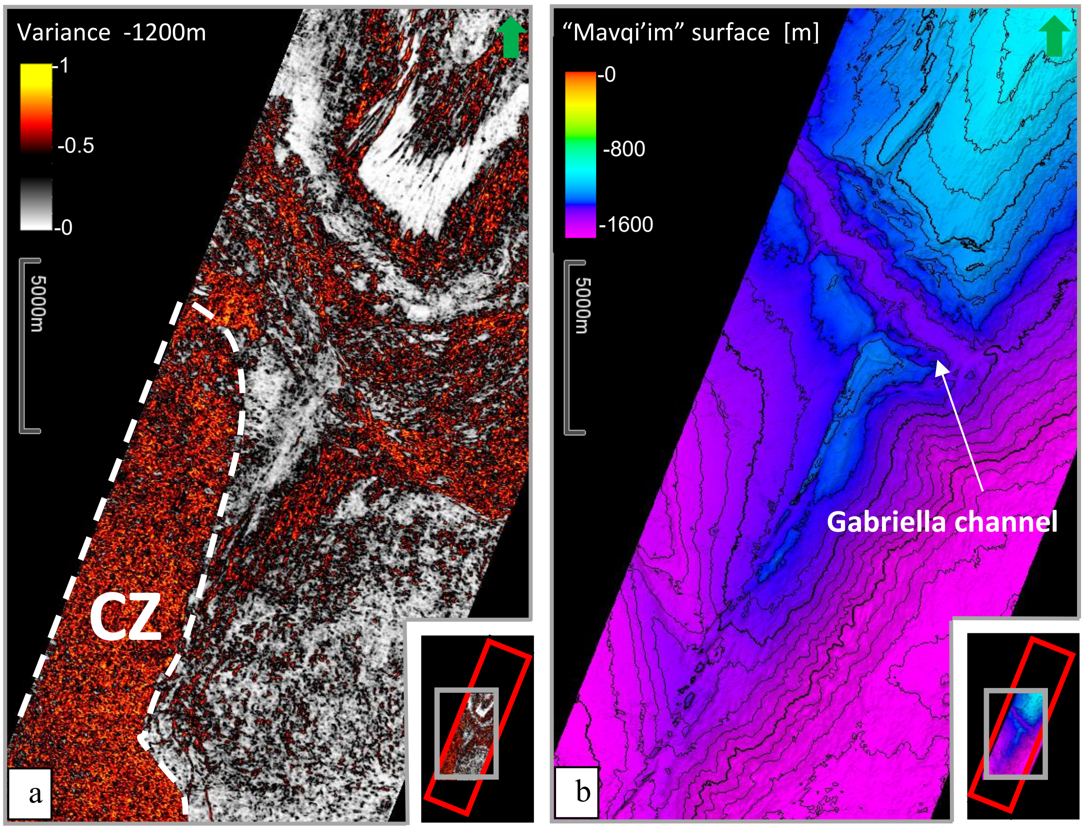

Figure 17. Predominant structures in the "Gabriella" survey. (a) Variance depth slice at -1200m highlighting the Chaotic Zone extent. (b) Structural map, top "Mavqi'im" Fm. The Gabriella channel cuts through the "Gabriella-Yizhak" anticline.

The Plio-Pleistocene sequence is characterized by continuous reflections with intervals of weak reflections (Fig. 18). The thickness of the sequence exceeds 1000m at the western part of the survey, terminating eastwards as pinchouts, representing progradational sedimentation (Lang, 2016). Ten key horizons labeled *a-i* are mapped for displacement analysis (Fig. 18). These are bounded by two horizons representing the Sea bottom and the Mavqi'im formation, labeled *SB* and *M*, respectively.

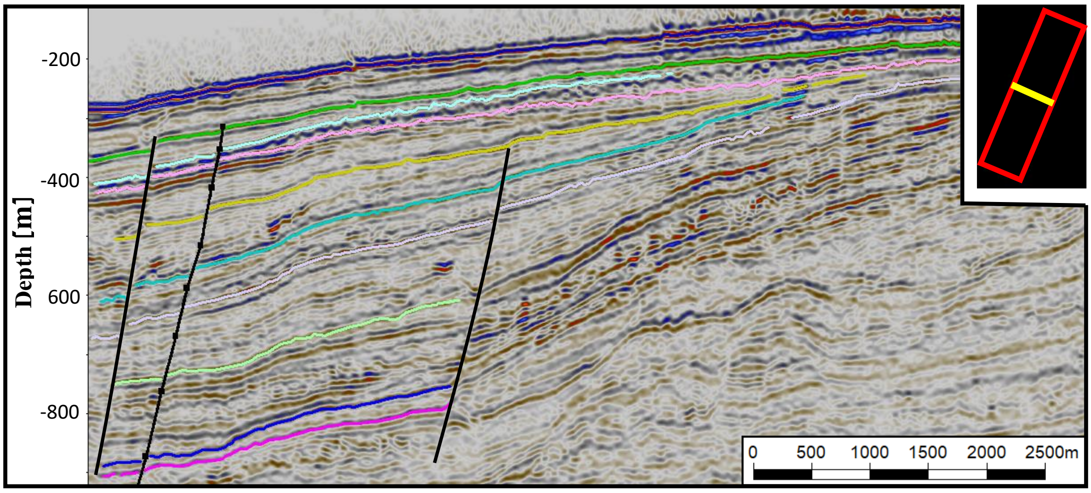

Figure 18. "Gabriella" Stratigraphy settings (Crossline 3840). Key horizons a-i are colored, increasing thickness towards the west, and terminating as pinchouts in the east. Strong reflections are interbedded with weak reflections. Faults are marked with black lines (with black squeres- Fault used for throw analysis).

Dozens of normal faults dissect the Plio-Pleistocene sequence. Two main fault zones are identified (Fig. 19a): a northern fault zone (NFZ, Fig. 19b) and a southern fault zone (SFZ, Fig. 19c). The NFZ comprises N-S striking faults accompanied by synthetic faults. Some of the faults are crossed by E-W normal faults. The zone is terminated by a pinchout to the east, and by the CZ and its overlaying sequence to the south. The SFZ is comprises NW-SE striking faults, accompanied by synthetic and antithetic faults, and is bounded by the chaotic zone and its overlaying sequence to the north.

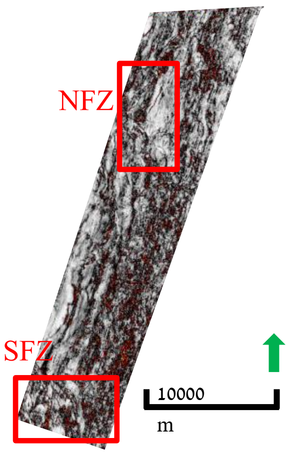

Figure 19a. "Gabriella" license fault zones. NFZ & SFZ on -464m variance depth slice.

Some faults in the northern region of the survey cut through the *M* reflector, showing displacement values reaching up to 50m. In the southern region, M is faulted at the CZ basal shear zone show displacements reaching up to 100m.

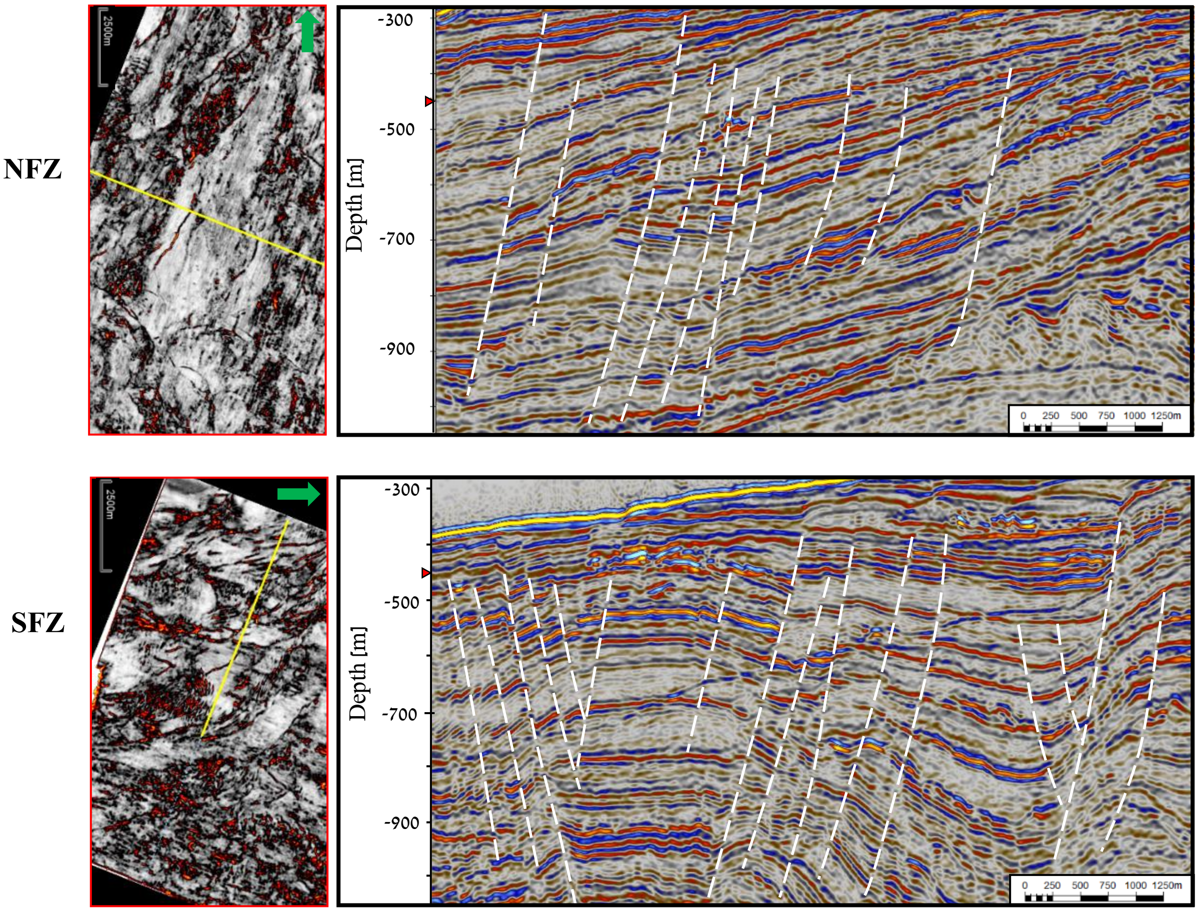

Fig 19b. (left) NFZ and SFZ map view with Variance depth slice from -464m. Yellow lines- cross sections from both sections view on the right. (right) Up- NFZ normal and synthetic faults. Bottom- SFZ normal, synthetic and antithetic faults.

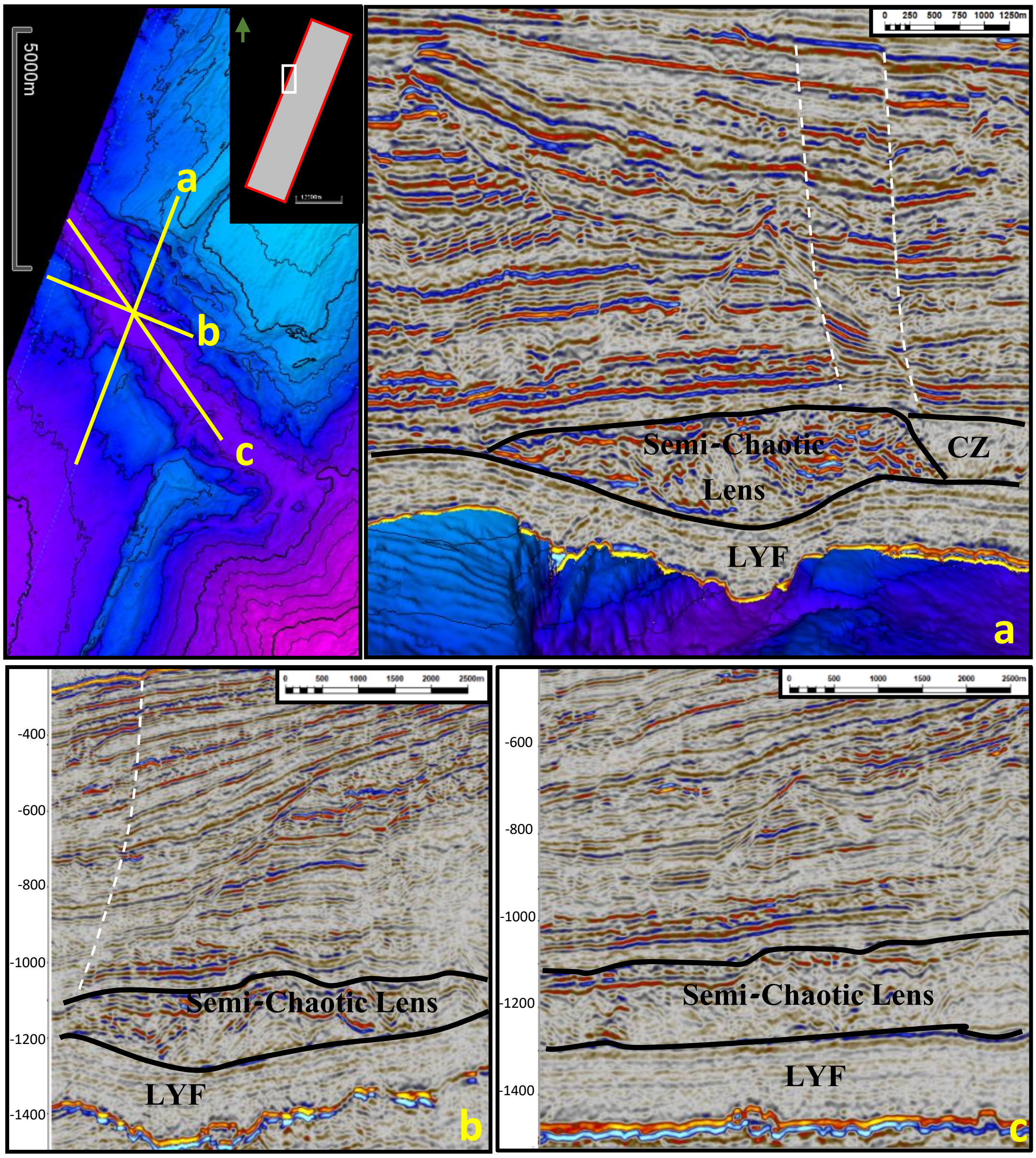

Figure 20. The semi-chaotic lens. (a) Inline 1092. LYF filling the "Gabriella" channel, underlying the semi-chaotic lens. White dashed lines- faults striking E-W, bounding the CZ northern edge (northern edge?). (b) Crossline 3144. The section cuts through a longer section of the lens. White dashed line - Fault 1, analyzed for displacement patterns. (c) View of a random line crossing the "Gabriella" channel.

4.2 Displacements analysis

Four faults situated in the NFZ whose key horizons are traceable were picked for displacement analysis, thus producing displacement measurements (Table 1). However, some chaotic and/or weak reflections generate an unclear contact between the hanging and foot walls in different parts of the faults. The lower section of the seismic section between 800-1200m depth is characterized by longer wavelengths thus reducing the vertical resolution (see chapter 2.1.1). This results in four key effects:

- Fewer displacements are measured, with greater gaps between them, limiting reliability of T-Z plots classification as either C/M types.
- Most key horizons represent the upper part of the faults.
- DCD plots are subjected to more interpolation bias at their lower part.
- Vertical displacement gradients (hereafter displacement gradients) for all faults are calculated for the upper part of the faults' surfaces, with maximum displacements referring to measurements at 400-800m depth.

Aspect ratios for all four faults range between 1.47-1.6, insufficient for classifying them as either vertically or horizontally restricted. They all show similar W vs. D relations (Fig. 21) and mean displacement gradient values of < 0.1, as expected for faults with strike dimensions of 1.3-9.7 km (Nicol et al., 1996).

Fault #	Displacement measurements #	Total crosslines Intervals	Interval Size [m]	Width (2R) [m]	Maximum Displacement [m]	Mean Dis Gradient	A.R
1	508	28	62.5	1937.0	46	0.04	2.09
2	342	9	62.5	1137.0	47	0.08	1.4
3	633	36	62.5	2312.0	49	0.04	2.4
4	501	33	62.5	1312.5	49	0.07	1.4

Table 1. Displacement and dimension measurements of NFZ faults used for this research.

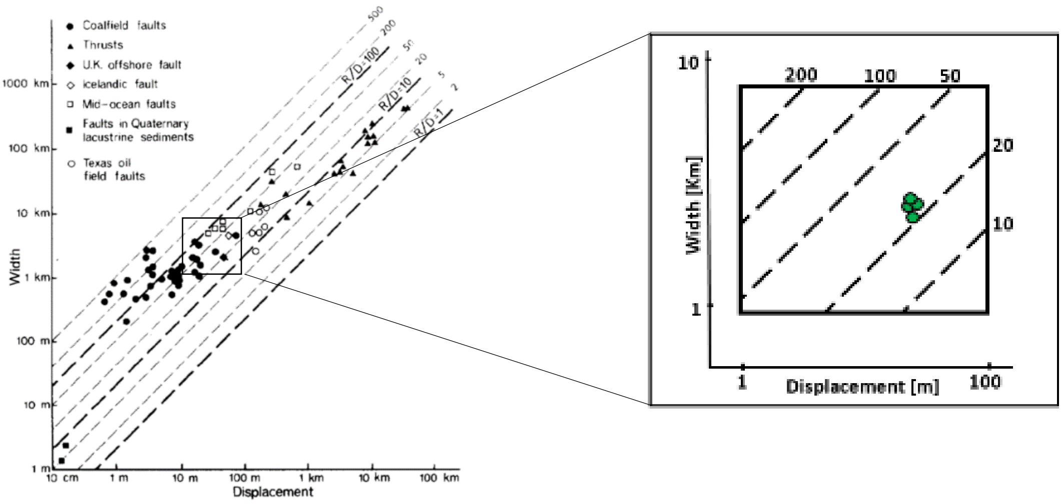

Figure 21. The four NFZ faults plotted on Displacement Vs. Width graph. Modified after Barnett et al. (1987). The cluster (green circles) suggests the NFZ is generally characterized by normal faults with ~50m maximum displacements, and 1-3 km width.

Faults 1-3, all at the NFZ's southern part (Fig. 22), yield different displacement patterns despite their close proximity.

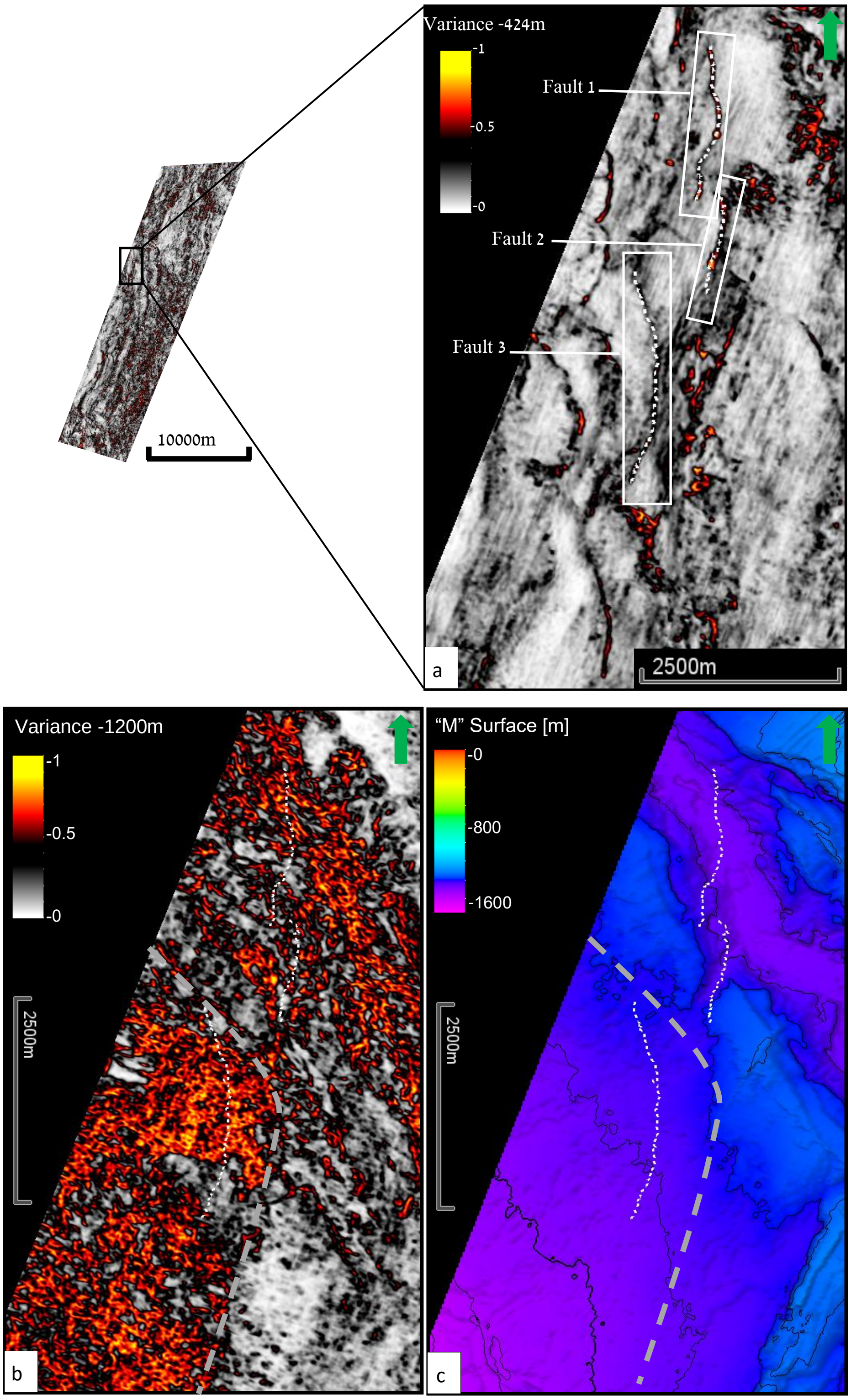

Figure 22. Faults 1-3 location maps. (a) Faults 1-3 on variance slice at -464m depth. (b) The CZ with relation to the overlaying faults. Gray dashed line - CZ northern boundary trace at -1200m. (c) The "Gabriella" channel with relation to faults traces projected from -464m (White dashed lines). Gray line - The CZ northern boundary.

4.2.1 Fault 1

Fault 1, above the semi-chaotic lens, is 1850m wide and 885m long, resulting in an aspect ratio of 2.09. The fault's bottom part comprises the northern flank of a chaotic body incised into the lens, which is interpreted as a slump structure (Fig. 23). The slump, limited to the survey area, is 750m wide, 500m long and ~ 200m thick. The chaotic characteristics suggest the slump is part of the ISC.

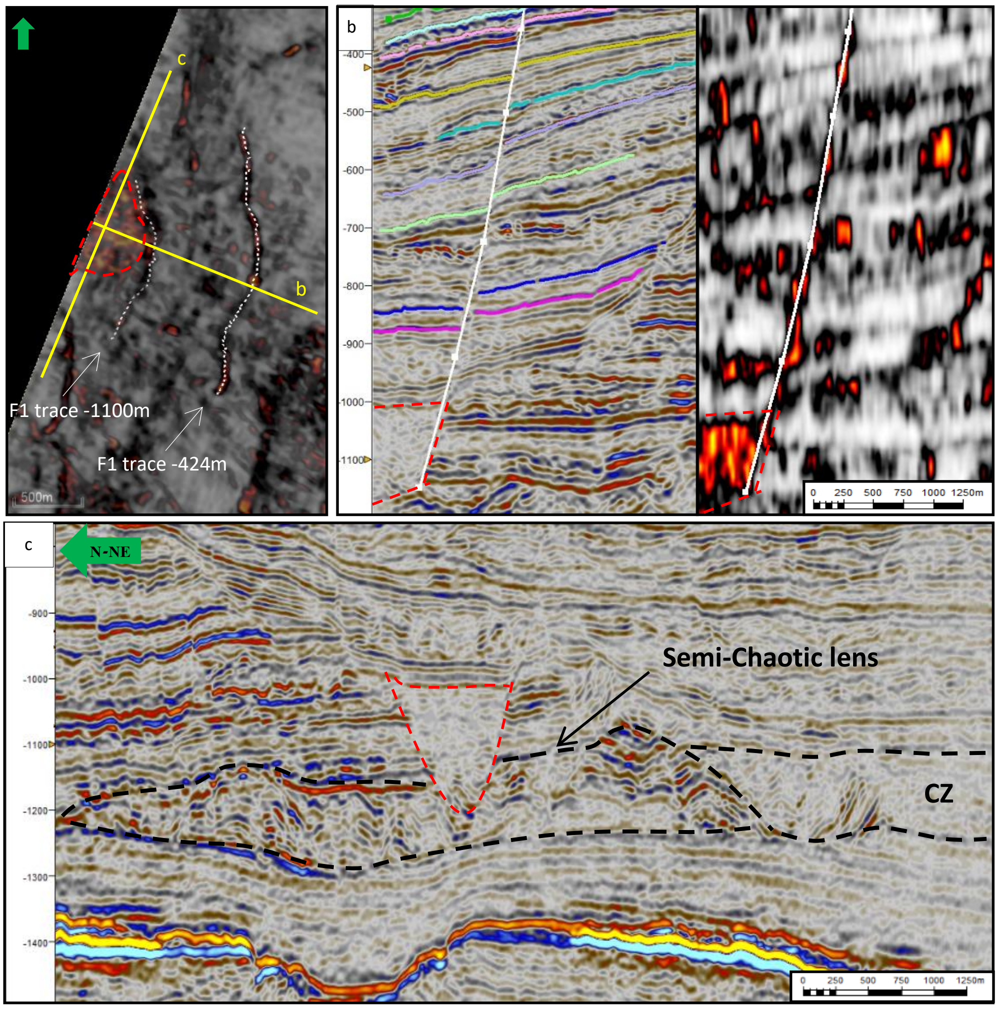

Figure 23. The chaotic graben. (a) Half-transparent variance slice at -424m over a -1100m variance slice. The map presents Fault 1 traces at the different depths. Red dashed boundary - the graben structure as seen at -1100m. (b) Crossline 4085 cross section with key horizons and variance cross section. Fault 1 incised the graben. (c) Inline 1012 cross section, presenting the chaotic graben incision of the semi chaotic lens.

T-Z plots record vertical and lateral fault tips, excluding the lower part of the graben zone, e.g. crosslines 4175, 4195 (Fig. 24a). Most plots do not exhibit consistent patterns of either C or M type. The central part features bimodal displacement patterns, where two displacement maxima are measured at different depths (e.g. crossline 4195, Fig. 24a,b). The first maximum displacement is measured at ~550m depth. The second maximum, which is also the largest, is measured at ~1000m depth, right above the slump zone. The vertical gradients average 0.087, measured at 597m 58m depth (Fig. 24c.

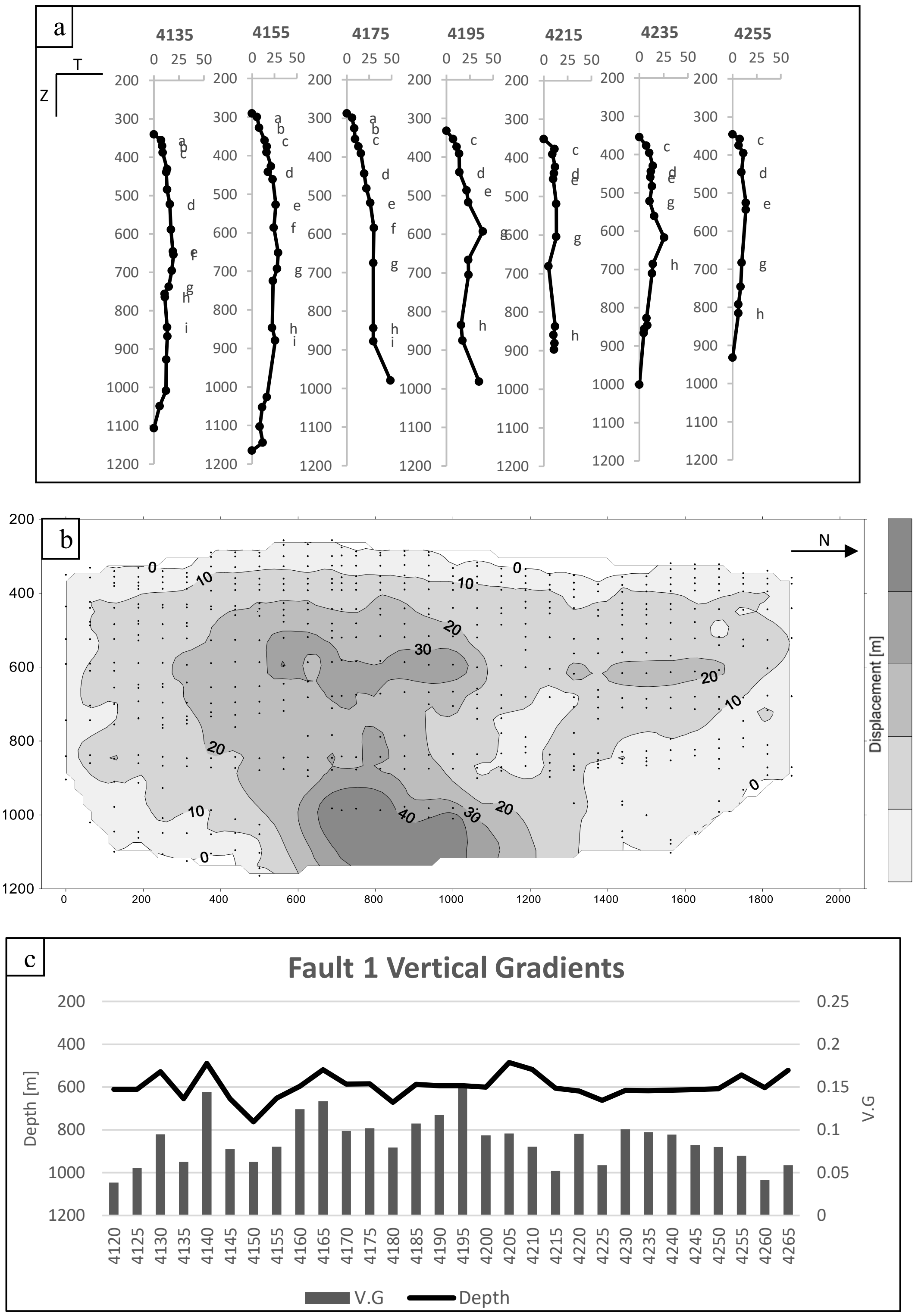

Figure 24. Fault 1 displacement patterns. (a) T-Z plots along the fault surface with 20 crosslines (250m) interval. The central plots (4175, 4195) are characterized by displacement increase with depth. (b) Displacement contour diagram. The irregular shape suggests the fault developed in a restricted manner. (c) Vertical gradients, averaging 0.087at 597m depth.

T-Z plots 4165,4185,4190,4205 (Fig. 25; Appendix) exhibit stepped intervals initiating at horizon *e*, indicating a localized growth stage or an active segment within the central part of the fault controlled by the chaotic graben. Accordingly, *SB* horizon shows increase in curvature, limiting this segment between crosslines 4132-4193 (Fig. 25).

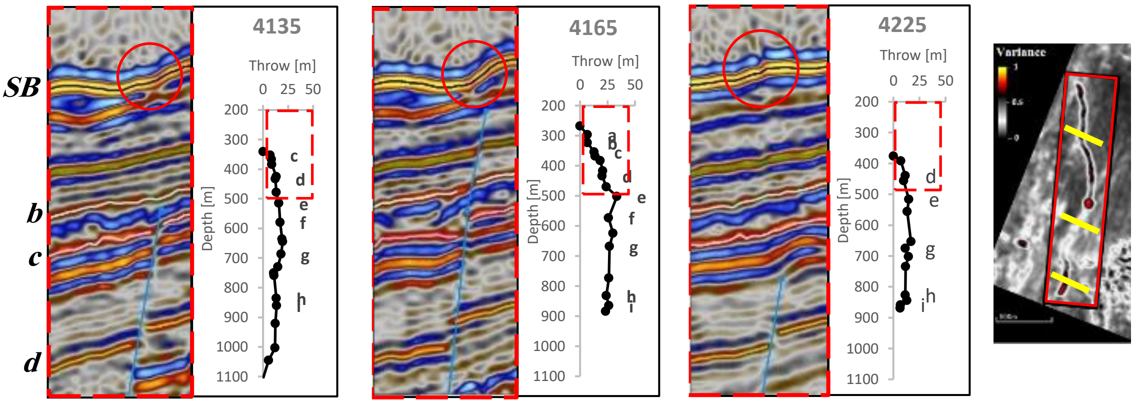

Figure 25. Sea Bottom (SB) curvature variations above fault 1. The central 4165 crossline, at the chaotic graben area, presents a stepped T-Z profile together with a curvature increase of the "SB" horizon (red circle), indicating local activity. Notably the northern and southern crosslines exhibit neither stepped profiles nor high curvature.

T-Z plots from the northern part of the fault exhibit local spike patterns where key horizon *f* shows an abrupt increase in displacement values as compared to horizons *e,g* (crosslines 4230, 4220, Fig. 26). In this part, *f* also represents maximum displacement values. The southern part, however, is characterized by moderate displacement variations between horizons *e,f,g* (crosslines 4150, 4170, Fig. 25). In both areas, *f* shows similar displacemen t values, therefore the spiking patterns are credited to the low displacement values of the *e,g* horizons. In the northern part, these horizons are overlying traceable, strong amplitudes whereas in the southern part they are underlain by semi-chaotic reflections. This suggests that the stronger reflections in the northern part represent a denser unit, more resistant to shear.

The differences between T-Z plots from the northern, central, and southern part is also evident in the DCD plot: A 20m contour at the northern part is separated from the central maximum displacement zone by a 10m contour at 1200m distance on the fault surface in Fig 24b. This suggests that the fault evolved by merging of two separated faults as illustrated by the fault growth models (Fig. 7).

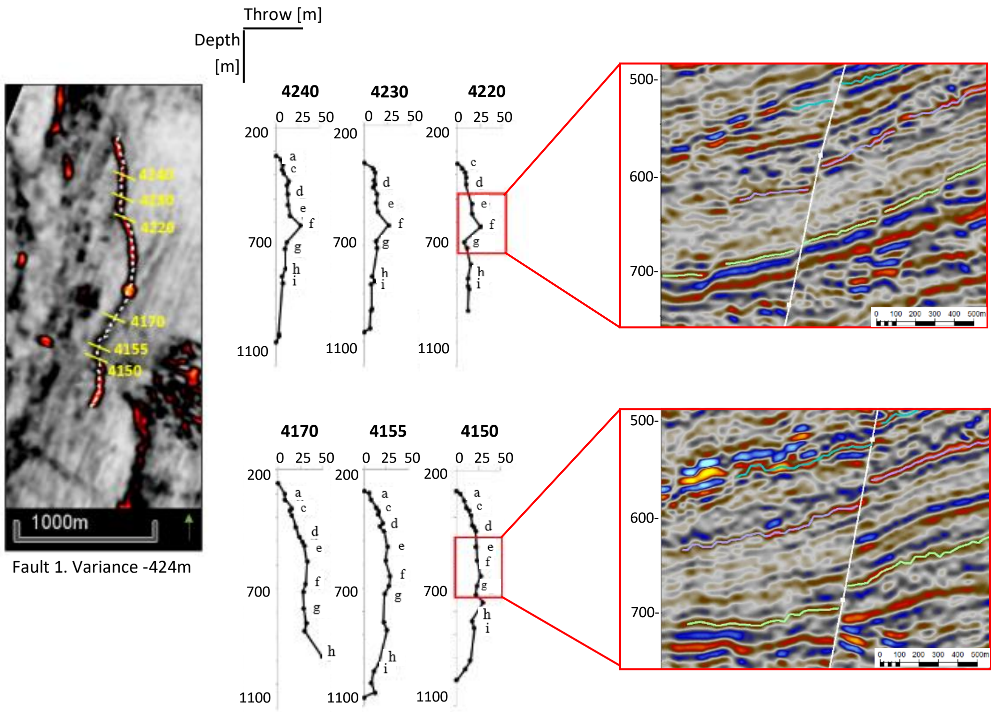

Figure 26. Fault 1 T-Z plots variations. Northern crosslines 4240,4230,4220 (up) exhibit a spike pattern at key horizon "f", that is not observed in the southern 4170, 4155, 4150 crossline (bottom). This could be due to local changes in lithology, as crossline 4220 shows weak reflections between horizons f-g, possibly representing a weak unit as compared to a stronger unit in the southern part, characterized by continuous reflections in crossline 4150.

4.2.2 Fault 2

Fault 2, also above the semi-chaotic lens, is adjacent to faults 1 and 3 and is bounded by the chaotic zone and its overlaying strata on the south. The width and length are 1200m and 841m respectively, resulting in an aspect ratio of 1.4. T-Z plots exhibit asymmetrical C-type (Fig 27a). Maximum displacement values measured at the central part of the fault indicate blind propagation, exhibited by the DCD's 40m contour zone (Fig. 27b). Low A.R. and similar displacement gradients in both the horizontal and vertical directions also indicate unrestricted propagation. Vertical gradients average 0.092 at 572m ±78m depth (Fig. 27c). Despite a decrease in displacement to 0 at the bottom part, it seems that in the central area the fault incises deeper into the "Mavqi'im" where measurements are not possible.

4.2.3 Fault 3

Fault 3 incises the northern part of the CZ (Fig. 22). Fault width and length are 2475m and 1030m respectively, resulting in an aspect ratio of 2.4. The central area of the fault shows root traces incising the *M* horizon.

Most T-Z plots exhibit irregular patterns (Fig 28a; Appendix 3). Stepped profiles initiating at horizon *e* are identified at the fault's center, e.g. crosslines 3995, 3945, 3845

(Fig. 28a). Additional crosslines exhibiting stepped profiles are: 3880, 3915, 3935, 3940, 3945, 3955, 4010, 4005, and 3960 (Appendix).

The fault exhibits an asymmetrical, syn-sedimentary displacement pattern by closely spaced horizontal contours at the upper DCD, changing abruptly to sub-vertical (Fig. 28b). Maximum displacements form a small 40m contour zone, situated in the central-upper area of the fault, at ~450-575m depth. Contours in the bottom part don't show full closure due to the fault's incision into the CZ, where displacement measurements are not available. However it is clear that compared to the upper part this area is characterized by moderate displacement gradients, as expected for syn-sedimentary faults. Throw contour islands are scattered around the diagram and follow local throw variations, also recorded in the T-Z plots. For example, maximum throw measured at the bottom part of crossline 4020 resulting in a 20m contour interpolation (Fig. 28b). This and other contour islands anomalies, derived from small differences in displacement, might also relate to limitations in resolution.

Interpretation of growth initiation is marked by a dashed line at the contours' inflection points, following a technique after Childs et al. (2002, Fig. 14d). Comparing to the seismic data, growth initiation is interpreted between horizons *d-e*. Vertical gradients show an average of 0.12 at an average depth of 480m 45m, shallower than faults 1 and 2 (Fig. 28c). These observations suggest the fault evolution is controlled by the chaotic zone, which caused it to transition from blind to growth.

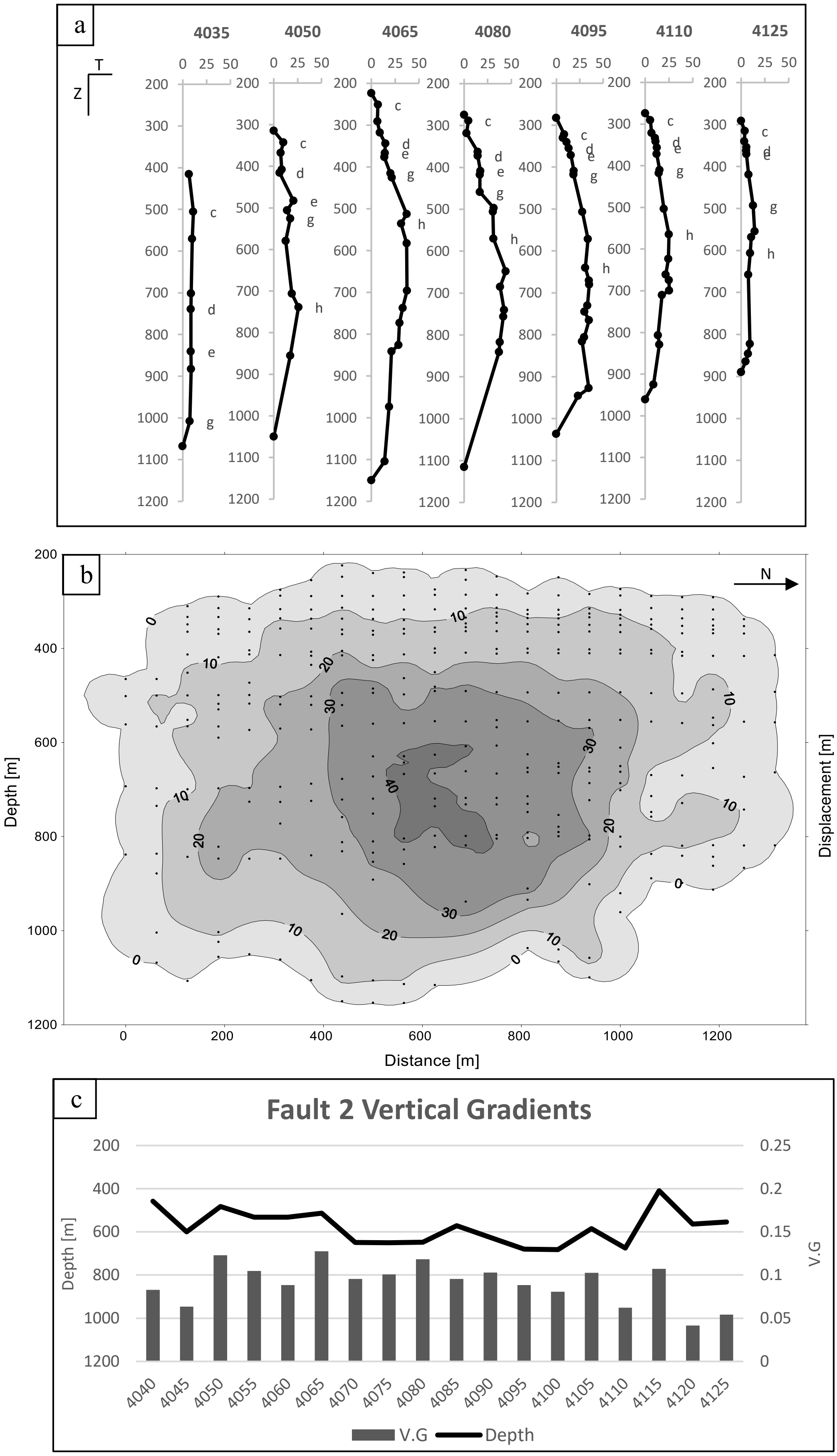

Figure 27. Fault 2 displacement patterns. (a) T-Z plots record the fault closure area at depth. (b) DCD presenting a blind development; similar vertical displacement gradients, together with maximum displacement at the fault center. (c) Vertical gradients diagram. 5 Crosslines (62.5m) horizontal spacing.

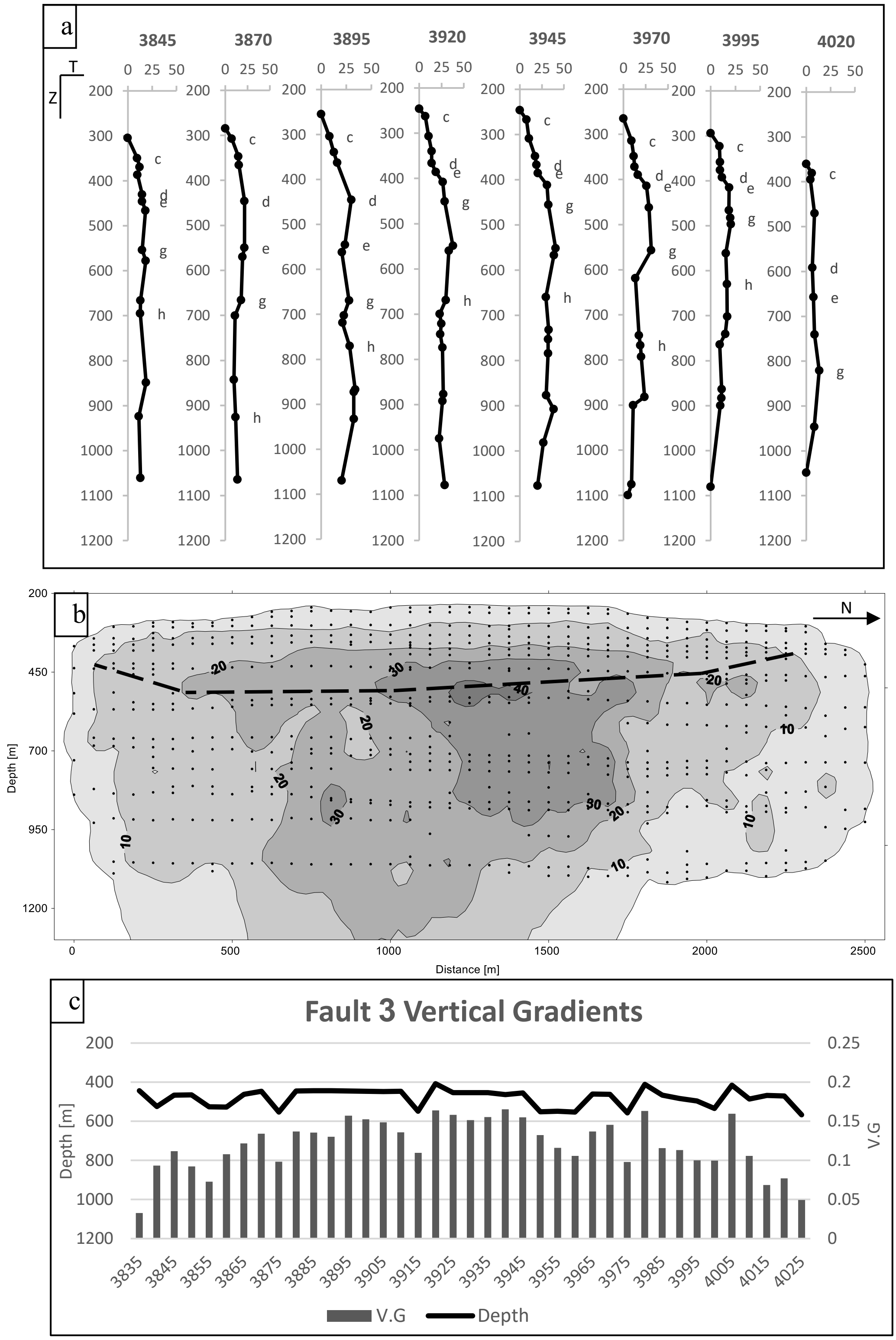

Figure 28. Fault 3 displacement patterns. (a) T-Z plots. (b) Closely spaced contours in the DCD upper part indicate a growth stage. Dashed line crossing the contours' inflection points from sub-horizontal to sub-vertical suggests the area of transition to growth (technique after Childs et al., 2002). (c) Vertical gradients plot. 10 Crossline (125m) horizontal spacing.

4.2.4 Fault 4

Fault 4, at the northern part of NFZ, ruptured above the western flank of the "Gabriella-Yizhak" anticline (Fig. 29). Key horizons *a-i* reach shallower depths in this area as compared to Fault 1-3. Therefore, deeper horizons *4a-4g* are mapped for displacements measurements (Fig. 30).

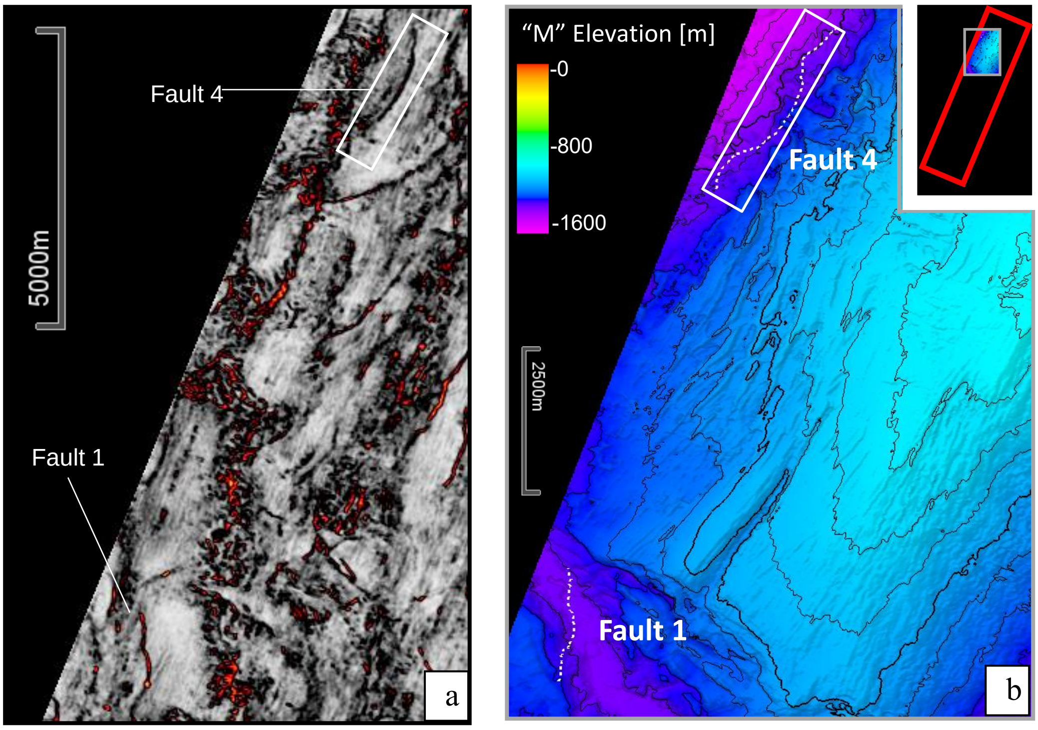

Figure 29. Fault 4 location map. Fault 4 location map. (a) The fault scarp on variance at -464m depth. (b) The fault projection, with relation to the underlying "Gabriella-Yizhak" anticline, as seen on the M structural map.

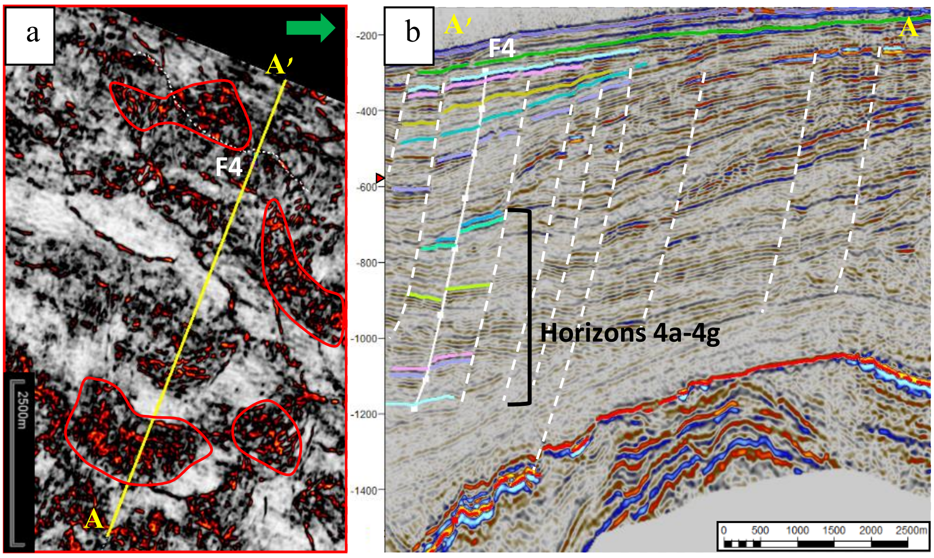

Figure 30. Fault 4 environment. (a) Variance at -592m delineating the characteristics of the NFZ environment. Semi-chaotic areas (enclosed in red) represent areas of discontinuous reflections. Yellow line is the trace of the section on the right. (b) Crossline 5010: Fault 4 among a series of synthetic faults. Key horizons a-f terminate at shallower depth of ~600m. Additional horizons 4a-4g are mapped for Fault 4 displacement measurements.

The throw pattern fits neither blind nor growth faults (Fig. 31a) based on the following observations from the DCD:

The bottom part presents closely-spaced 0-20m contours, implying vertically restricted settings. The central part of the diagram shows numerous 40m contour islands at ~600m depth due to a lack of measurements. This implies the fault cuts through a chaotic body. Two 30m contours at the sides of the diagram are interpreted as nucleation zones from linked faults.

The vertical gradients diagram highlights the linked zones, distinguishing the three faults (Fig. 31b). Vertical gradients from the central part of the diagram range from 0.07 to 0.1 at 730-810m depths, setting the fault's horizontal limits between crosslines 4915-5020. A gradient peak in crossline 4965 seems to represent the fault nucleation point, situated at the center of the 40m contour islands. According to these measurements, Fault 4 shows an A.R. of 1.42 and mean displacement gradient of 0.074, agreeing with the indices suggested by Nicol et al. (Chapter 1.3.1). Interpretation of several variance depth slices reveals the linked zones, i.e. relay zones (Fig. 32), and also the slump structure (Fig. 33) between 500-700m depths which results from interpolation of the 40m contour islands.

The linked faults are characterized by higher gradients, ranging from 0.15 to 0.2, measured at shallower depths of 550-650m. In contrast to Fault 4, maximum displacements within the linked faults result in only 30m contours and also seem to nucleate at a shallower depth. Both linked zones show gradients increasing as compared to those measured (0.1, 0.12) at fault tips in the southern zone (crosslines 5030, 5035), and 0.21, 0.25 in the northern zone (crosslines 4900, 4905). The latter is also detected by the large tongue of the 30m contour reaching over 1000m depth (at 750-1000m distance axis, Fig 31a).

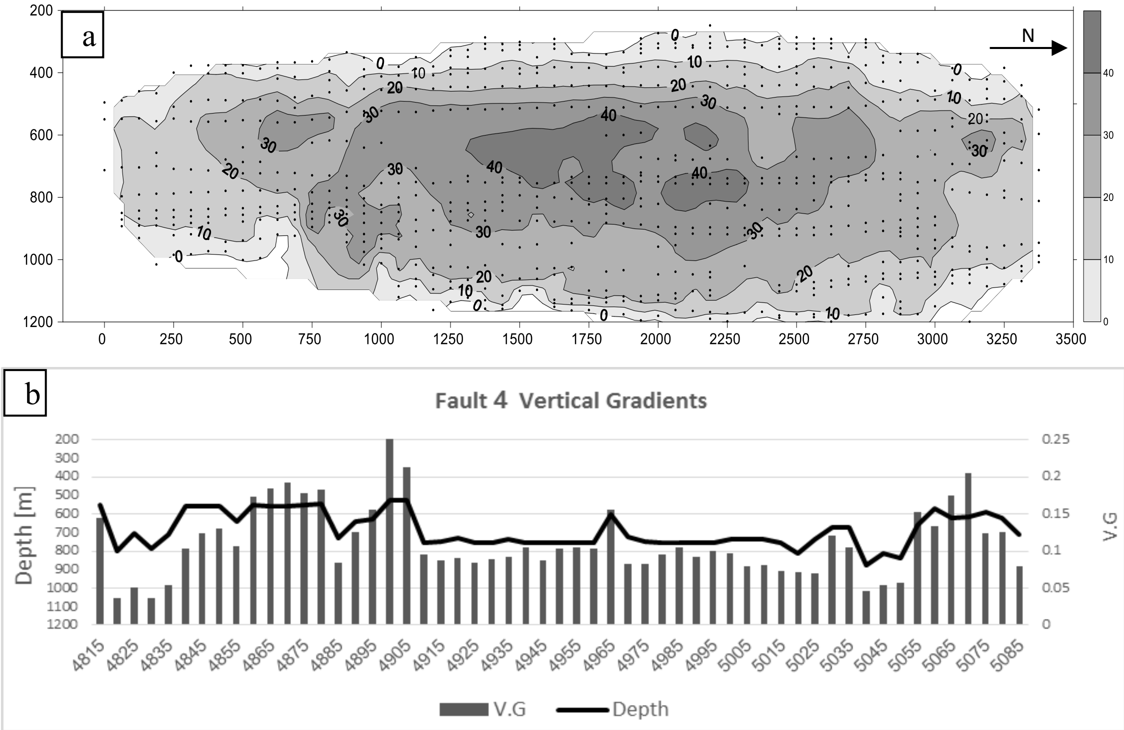

Figure 31. Fault 4 DCD and V.G diagrams. (a) DCD exhibits fault linkage with two adjacent faults at 750-1000m and 2750-3000m. The 40m contour islands in the central part likely an artifact of gaps in measurements. (b) V.G. plot. The peak in gradient values at crossline 4900 correlates with the area of the 30m contour tongue and the fault's northern linkage.

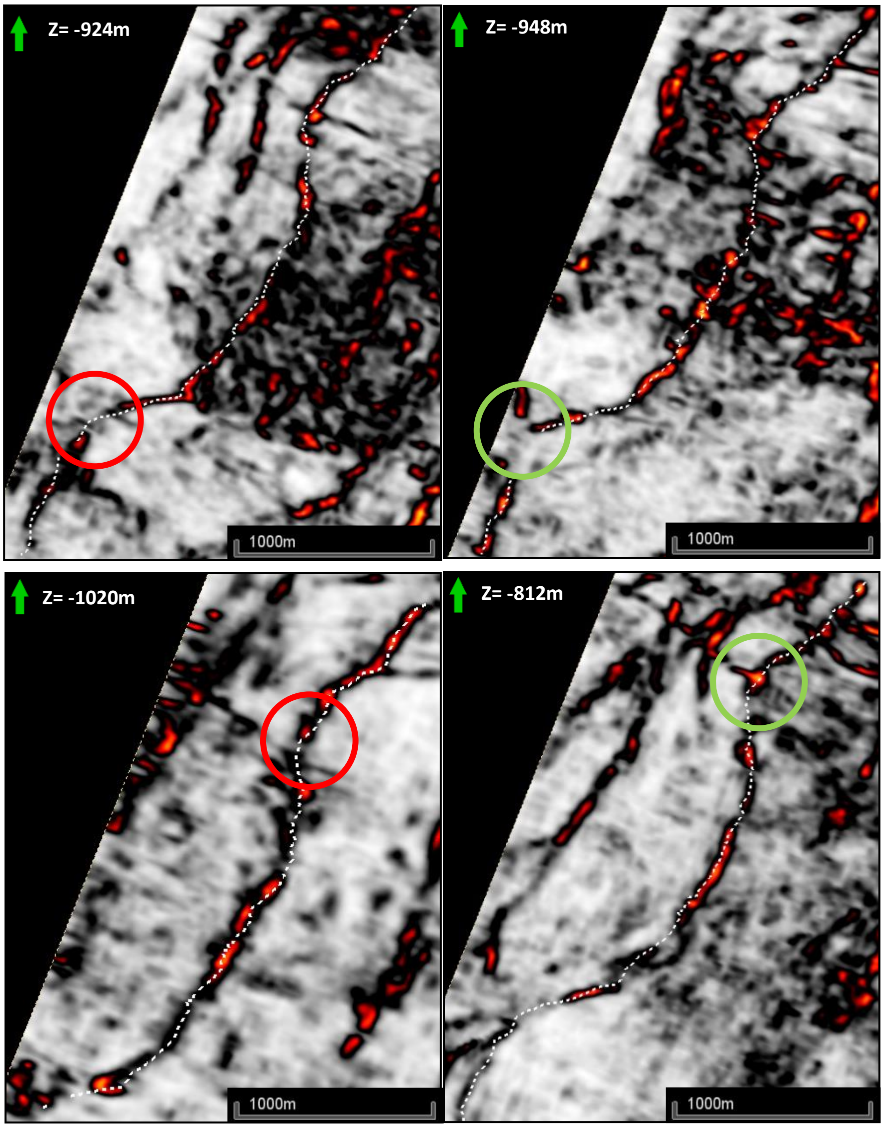

Figure 32. Fault 4 boundaries correction. Red circles- False mapping where variance forms an image of a single fault. Revision after displacement analyses highlight fault linkage (green circles).

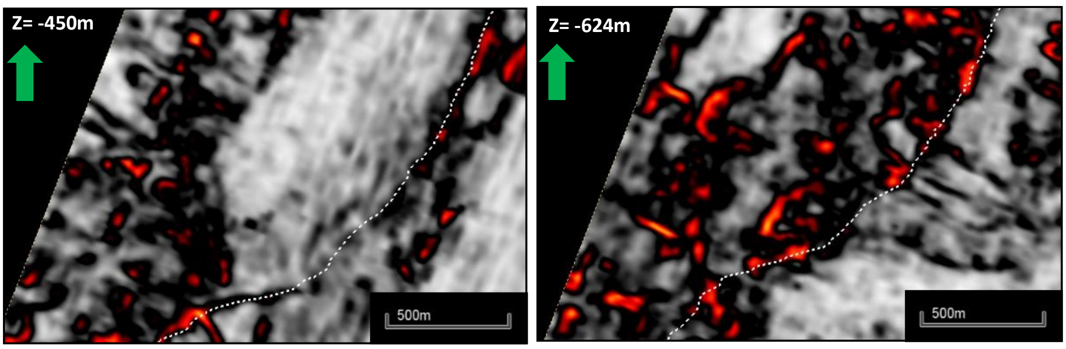

Figure 33. Chaotic unit crossed by fault 4. Variance depth slice at -450m exhibits clear zones at both the hanging and base walls of Fault 4. (b). Variance depth slice at-624m exhibits chaotic zones at both blocks, correlated with the blank zone of measurements at the fault's DCD between 550-650m.

4.2.5 Key horizons throw-strike projections

Variations in key horizon displacements delineate the propagation differences between the faults, especially between faults 2 & 3 (Fig. 34). Fault 2 exhibits a triangular throw shape with throw values generally increasing from *a* to *h*, indicative of blind development. This also sets the fault's nucleation zone at the *g,h* horizons. In contrast, Fault 3 can be divided into two groups: horizons *a-c* and horizons *d-h*, represented by low and high displacement values respectively. The groups are separated by a blank gap due to a lack of measurements between crosslines 3925-3970. This also correlates with an abrupt change in the 30m contour previously seen in the fault's DCD (Fig. 28b). The fault's maximum displacements are measured at horizon *e*.

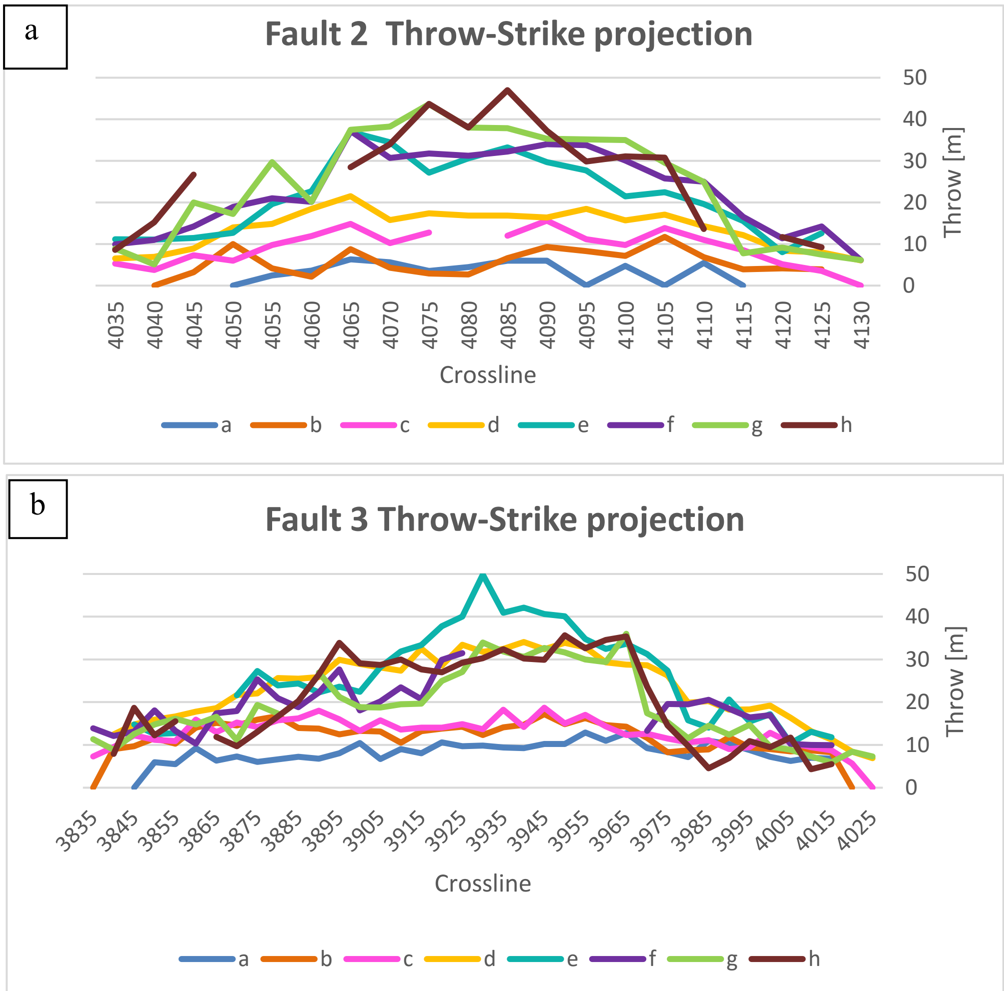

Figure 34. Throw-Strike projections for faults 2 & 3. (a) Fault 2 exhibits a triangular pattern, with maximum throws at horizons g,h, as expected for blind faults. (b) Fault 3 exhibits maximum throw at horizon e, and forms a blank window where horizon f is cutoff, suggesting a different evolution.

Restriction on Fault 1 by the chaotic graben results in scattered throw distributions at its central part (Appendix). This leads to higher uncertainty in the interpretation. Fault 4, despite cavities in throw measurements of some key horizons, shows a general displacement increase with depth similar to Fault 2, thus supporting its blind propagation interpretation.

4.3 Faults 2 & 3 restoration models

The central crosslines of faults 2 and 3, showing the largest thickness and displacement values, are restored (Fig. 35). These restorations are carried under assumptions of continuous sedimentation with no unconformities between the seismic packages, and no erosion processes during fault development. Fault ~~2's~~ restoration hardly indicates overlap of key horizons from the hanging wall over the footwall. Results from Fault 3 show minor overlap of horizons a,c following the flattening of horizon d (Fig. 35). This result agrees with a late growth stage. Flattening of e,f shows no indication of earlier growth stages.

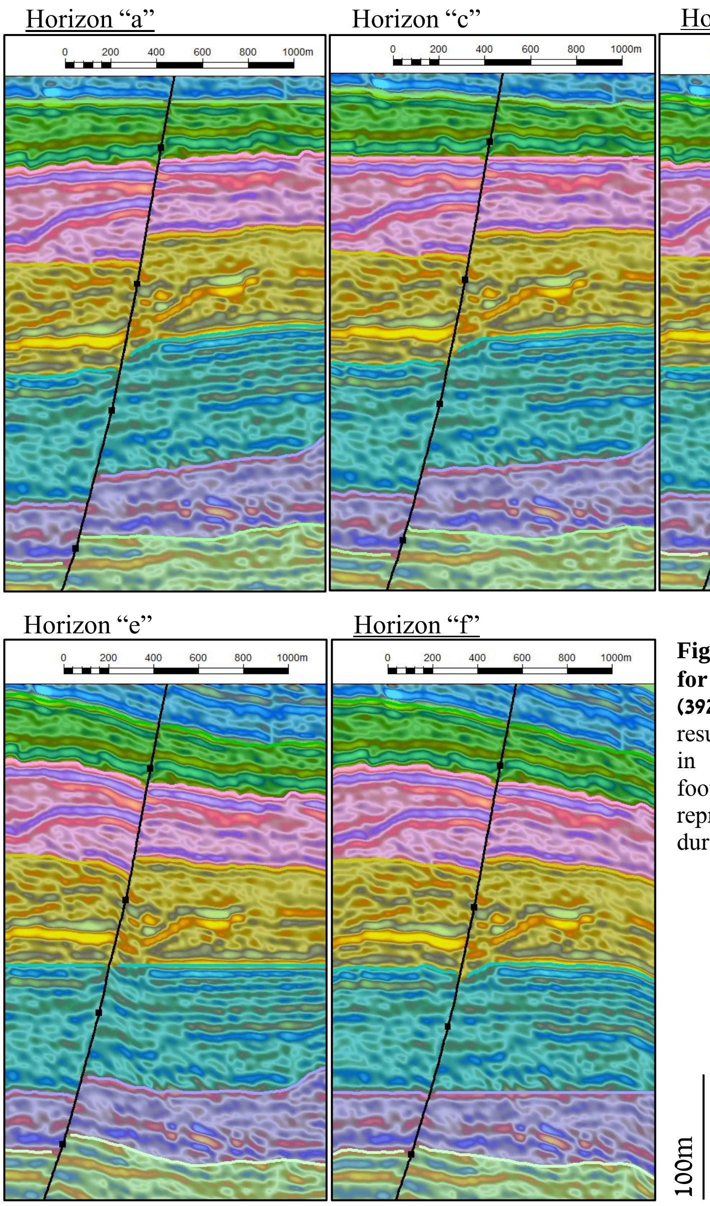

Figure 35. Restoration model for fault 3 central crossline (3925). Horizon “d” flattening results in overlap of key horizons in the hanging wall over the footwall (red circles), thus representing a growth phase during a-d sedimentation.

4.4 EI calculations and thickness variations of the seismic packages

Following the restoration models, EI calculations were carried out on the seismic packages of faults 2 and 3 (table 2, Fig. 37).

	Crossline	a-c	c-d	d-e	e-f	f-g
Fault 2	North	1.04	1.18	1.13	1.02	0.99
	Center	1.12	1.11	1.19	1.13	1.08
	South	1.06	1.13	1.18	1.13	1.01
	Average	1.07	1.14	<u>1.16</u>	1.09	1.02
Fault 3	North	1.1	1.21	1.11	1.12	0.98
	Center	1.0	1.32	1.13	1.06	0.92
	South	1.25	1.22	1.15	1.02	1.02
	Average	1.13	<u>1.25</u>	1.13	1.06	0.97

Table 2. EI values for seismic packages of faults 2 and 3.

Fault 2's southern and central crosslines show EI increase towards the center; from 1.06 and 1.01 to 1.18 at the south, and from 1.12 and 1.08 to 1.19 at the center, thus indicating blind fault propagation. The maximum value of 1.19 in the central crossline presumably accommodates the fault nucleation point and therefore is not credited to a growth phase. Instead, it suggests that blind fault propagation can exhibit high EI values, which one might assume to be growth related. Fault 3's deeper e-f and f-g packages are characterized by low EI values similar to Fault 2, averaging 1.06 and 0.97, respectively. The upper a-c, c-d, and d-e packages are characterized by higher values, reaching up to 1.32 in the c-d package. This combination of deep and low EI values, followed by shallow and high EI values, suggests that Fault 3 transitioned from blind to growth. The EI histogram (Fig. 36) suggests a boundary index of 1.2 between growth and blind stages in these settings.

.

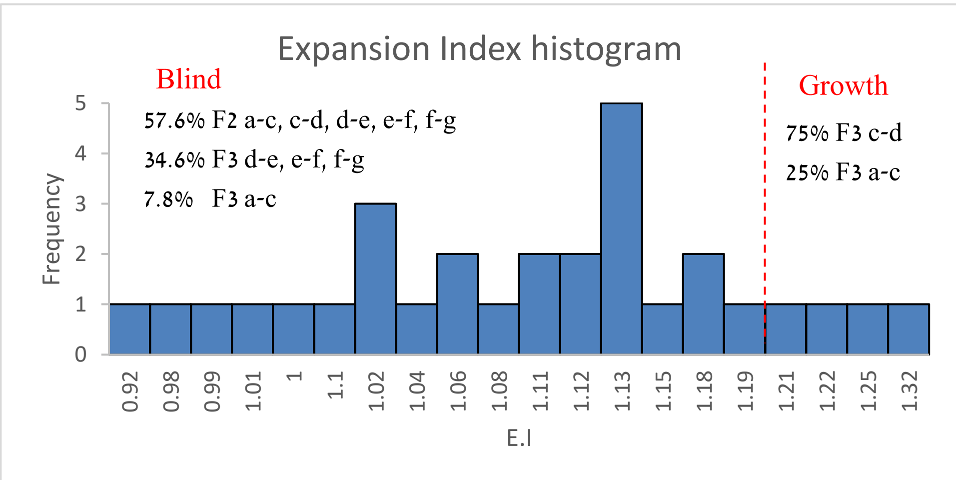

Figure 36. E.I histogram for fault 2 and 3 seismic packages. Red dashed line seperates blind and growth values. Measurments associated with growth are credited only to packages in the upper part of fault 3. Values from fault 3's bottom part represent 34.6% of the blind values, indicating the transition from blind to growth.

Thickness variations

Thickness variations in the seismic packages are analyzed for further spatial insights (Fig. 37). The Fault 2 packages are characterized by minor thickness variations, which together with generally low EI values indicate unrestricted blind propagation.

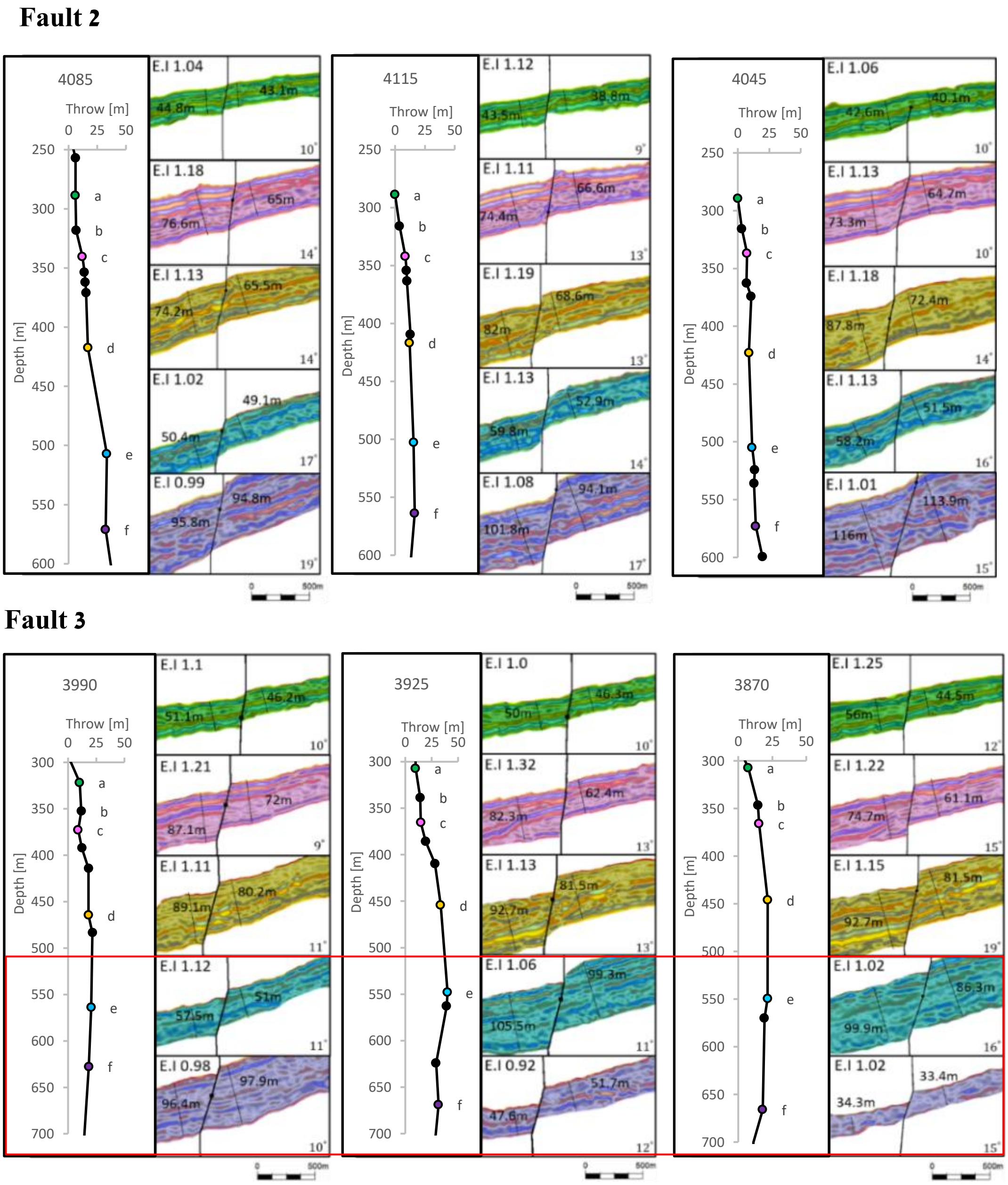

Figure 37. EI measurements for Faults 2 and 3 seismic packages. The packages dip at angles of 7-29° resulting in measurement uncertainty of 2-10%. The measurements were carried out close to the fault surface in order to eliminate, as much as possible, the influence of progradational sedimentation. T-Z plots are stacked against EI values to underscore correlation. The Fault 3 f-g package shows a decrease in thickness southwards with an increase in the depth of displacement measurements (bottom red rectangle).

Thickness variations in Fault 3's seismic packages allow dividing the fault into upper and lower sections as previously done in the EI calculations. The upper section, comprising *a-c, c-d, and d-e* packages, shows similar thicknesses on both sides of the fault walls. These suggest uniform sedimentation during growth stage. However, the lower section , comprising *e-f and f-g* packages, shows thickness increasing from 118m in the northern part to 147m in the central and southern parts (Fig. 37). The trend of thickness variation flips: while package *e-f* thins northwards, package *f-g* gets thicker. Despite these variations, EI values stay low.

This analysis of the seismic data reveals a minor fault, striking E-W and dipping south, crossing the bottom part of Fault 3 (Fig. 38). This fault acts as a boundary for the *e-f* and *f-g* thickness variations. This fault is interpreted as one which developed as a growth fault prior to Fault 3's nucleation. Thinning of the *f-g* package is interpreted as resulting from the compaction processes. The minor fault terminates in the *d-e* package and showing no influence on the thickness of upper packages.

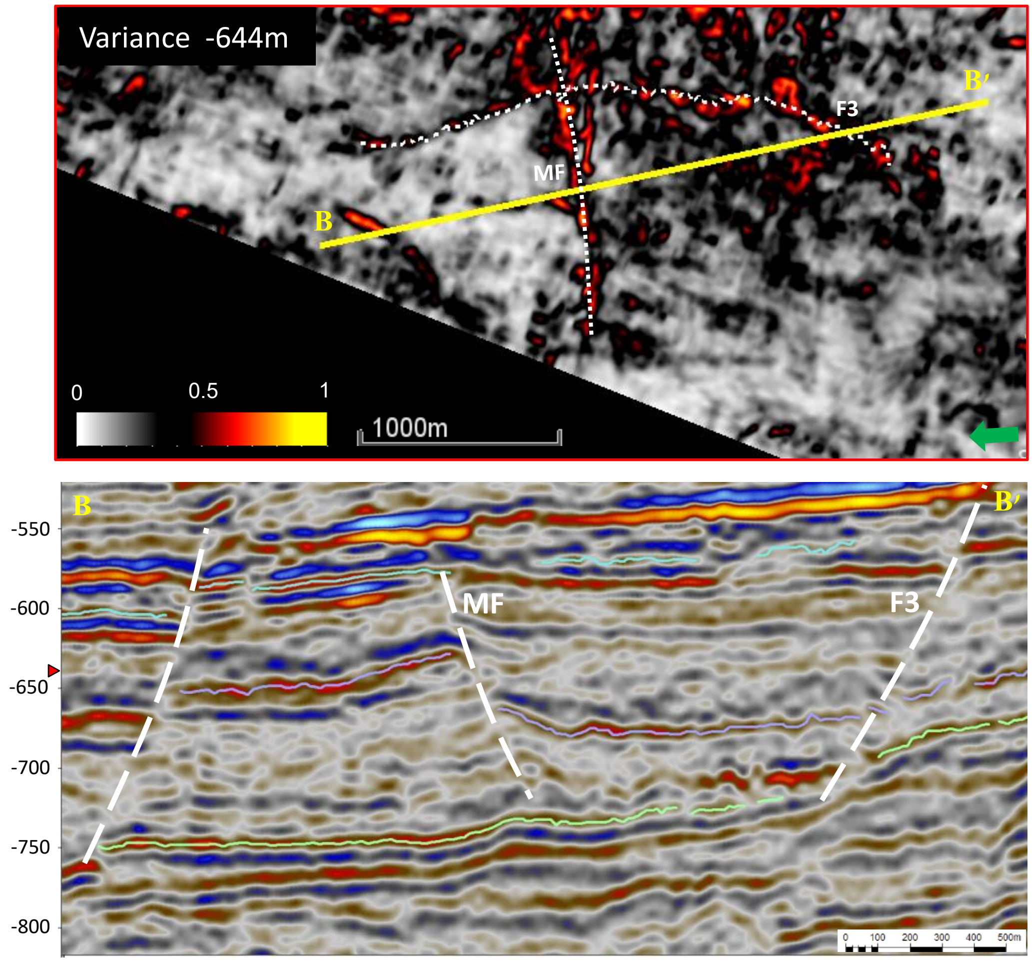

Figure 38. The minor fault. (a) Variance slice at -644m. The minor fault perpendicularly cross fault 3. An arbitrary line (yellow line) is drawn crossing both faults and an additional fault. (b) Cross section along the arbitrary line. Horizon "f" separates the e-f and f-g packages, both characterized by weakand chaotic reflections. These indicate the packages are disturbed and were not deposited in a conitnous manner. Fault 3's moderate dip derives from the wide angle of the section crossing it.

4.5 Growth initiation based on Yam- Yafo 1 and Romi 1 Well ties

Following interpretation of Fault 3 growth stages, stratigraphic data from the Yam-Yafo 01 and Romi 01 wells was examined for timing growth initiation.

Yam-Yafo 1

Located 5 km from the south-eastern boundary of the chaotic zone, the Pliocene section of Yam-Yafo 01 well was divided into biozones MPI 3, MPI 4, and MPI 5 by Druckman et al. (1994). Reflections following a well-tie by Paldor (2015) are not traceable towards the NFZ as most of them diminish above the chaotic zone. Despite this, the youngest biozone (MPI5), dated to 2.13 Ma, was tied to a reflector at 1150m depth. Therefore, it is likely that Fault 3' growth initiation, situated between 454 and 548m ,is younger.

Romi 1

Romi 1 is situated ~15 km east of the NFZ. Using chronostratigaphy and sedimentation rates from Lang (2016), horizon *G*, representing the top of the Gelasian stage (earliest Pleistocene). The horizon is mapped and dated at 1.8 Ma at 1100m depth, right above the CZ's northern part (Lang, 2016). Growth initiation according to the *G* horizon is calculated using 3 assumptions:

- Growth initiated at the d-e package.
- Sedimentation rate of 499 $[\frac{m}{Ma}]$ (Lang, 2016).
- Decompaction/compaction processes and lithological variations are neglected.

<u>Horizon "e" sedimentation age:</u>

$$\Delta Z = Z_{Gelasian} - Z_{horizon\ e} = 1100 - 548 = 552[m] \quad (10)$$

$$t_{sedimentation} = \frac{\Delta Z}{V_{sedimentation\ rate}} = \frac{552\ [m]}{499\ [\frac{m}{Ma}]} = 1.10\ [Ma] \quad (11)$$

$$1.8\ [Ma] - 1.1\ [Ma] = \mathbf{700\ [Ka]} \quad (12)$$

<u>Horizon "d" sedimentation age:</u>

$$\Delta Z = Z_{Gelasian} - Z_{horizon\ d} = 1100 - 454 = 646\ [m] \quad (13)$$

$$t_{sedimenation} = \frac{\Delta Z}{V_{sedimentation\ rate}} = \frac{646\ [m]}{499\ [\frac{m}{Ma}]} = 1.29\ [Ma] \quad (14)$$

$$1.8\ [Ma] - 1.29\ [Ma] = \mathbf{510\ [Ka]} \quad (15)$$

Following these calculations, fault 3 is interpreted as transitioning from blind to growth propagation at 510-700 [Ka].

5. Discussion, conclusions and summary

5.1 Restricted faults classification following displacement patterns

The four faults examined in the NFZ show similar characteristics regarding displacement values and fault dimensions (Table 1; Fig. 19). Also, the vertical extents of all faults reach over 1100m depth and terminate very close to the seafloor, implying that all faults evolved under similar geological settings. Therefore, differences in displacement patterns indicate restricted settings where fault propagation was controlled by geological structures. Faults 2 and 3 are classified as blind and growth faults for revealing the evolution of faults 1 and 4.

Fault 1 cannot be determined as blind, growth or a mixture of both from its irregular displacement pattern. The moderate gradients at the upper part of the fault, also illustrated by the contour spacing, resemble those seen in Fault 2. In addition, the maximum displacement zone identified by the 40m contour is situated at a similar depth to Fault 2. These observations suggest Fault 1 also propagated as blind before incising into the chaotic graben. The spike patterns (Chapter 4.2.1) suggest that the fault consists of 2 segments. This is supported by a small cutoff between the central and northern parts (Fig 22a).

Fault 4 is situated relatively far from Faults 1-3. Lack of measurements in its central part makes T-Z plots irrelevant for analysis, and cause more biased DCD interpolation. Vertical gradients allow determining of the fault boundaries. The bottom area of the fault, characterized by closely spaced contours, indicates vertical restriction. This observation rules out classification of the fault as unrestricted. The similar aspect ratio and vertical gradients to Fault 2 strongly suggests it developed as restricted blind (Table 1), and nucleated at greater depth. The fault abuts a series of normal synthetic faults which might be the cause of the restricted pattern. The underlying "Gabriella-Yitzhak" anticline (Fig. 29b) might also play a role in the restricted environment leading to the evolution of the synthetic faults. Variations between the low and high displacement values of the segmented faults, together with the high V.G. at linkage zones, fit the non-coherent isolated fault model (Childs et al., 2017). In accordance with these observations, Fault 4 is classified as blind-restricted.

All four faults are interpreted as having similar nucleation zones at ~600-700m depth exhibited by the 40m contours of faults' 1,2 and 4 DCD patterns. Fault 3's maximum displacement zone at ~500m is interpreted as resulting from the transition to growth fault and the migration of maximum displacements to shallower depth (Peacock, 1991; Baudon & Cartwright, 2008a).

Comparison of key horizon displacements along the faults' surfaces (Fig. 34) highlights the differences in the maximum displacement horizons. Faults 1,2 and 4 exhibit similar displacement increases towards deeper key horizons - *g and h* in faults 1 and 2 and *f and 4a-4i* in Fault 4. Fault 3 is the only one showing that maximum displacements are not only at shallower depth, but at the shallower *e* horizon as well. These observations support the hypothesis that the specific fault had a single growth phase. Analysis summary of the four faults indicate at least 3 different evolution types: Faults 1 & 3 - Restricted; Fault 2 - Blind Unrestricted; Fault 4 - Blind Restricted.

5.2 Distinguishing growth and blind phases using EI calculations.

Syn-sedimentary faults are accompanied by minor stratigraphic expansion (Thorsen, 1963). Blind faults can theoretically exhibit stratigraphic expansions as when stratigraphic expansion occurred prior to fault nucleation. Such a scenario is realistic in progradational settings, where sediment supply exceeds accommodation space (Catuneanu, 2016). The Plio- Early Pleistocene sequence in "Gabriella" is followed by Middle-Late Pleistocene progradational sedimentation initiated at 1.8 Ma (Lang, 2016), which makes distinguishing between blind and growth faults a challenge.

EI calculations for both faults 2 and 3 present mostly EI > 1 (Chapter 4.4), which could be referred to as being initially growth related. However, all the measured seismic packages are situated above the Galician reflector (Lang 2016) thus representing sedimentary units deposited under progradational settings. Variations in EI values between the two faults, even if minor, support the DCDs and restoration model interpretations separating blind and growth stages.

A growth criteria of 1.2 is set for identifying growth units in these progradational settings. Based on two faults quantitative analysis, this case study demonstrates how the proposed workflow can provide empirical evidence for fault classification.

5.3 Chaotic structures and their linkage to faults control fault evolution

Results suggest that fault evolution dominated by chaotic features. These features are divided into 2 types: chaotic bodies, such as the CZ and the chaotic graben; and the chaotic unit situated between continuous reflectors, i.e. between stratified layers.

Chaotic bodies

The CZ is derived from numerous slumping events (Paldor, 2015), which were interpreted to consist of weak material characterized by low shear strength. It is suggested that the initial blind propagation rate of Fault 3 was enhanced, following its

CZ incision, resulting in growth initiation. The second chaotic body - *the chaotic graben* - is interpreted as an Early Pleistocene slump unit controlling Fault 1 evolution. The irregular displacement pattern (Fig. 24) suggests the fault propagated as unrestricted blind before encountering the weak graben material, only at its central part. This resulted in a local activation phase within the fault, evident from the increased curvature of *SB* horizon. The two high maximum displacement zones support this interpretation, as maximum displacements are observed right above the graben, i.e. close to the restricted body. It seems unlikely that the fault initiated at the graben zone or below it, as in these cases, a steady upwards decrease in displacement values was to be expected.

The control of chaotic bodies depends on their spatial relationships with the faults: Fault 3's entire bottom edge incises the CZ, causing uniform growth transition, whereas Fault 1 incises the graben only in its central part, resulting in a local activation zone.

Chaotic units

Chaotic units also affect displacement patterns, yet their influence on fault evolution is minor compared to the chaotic bodies. Chaotic units identified in faults 1 & 4 are identified by local displacement variations, yet these are negligible compared to those associated with chaotic bodies. Additional chaotic areas in the Plio-Pleistocene sequence, irregular displacement variations in T-Z plots (Crosslines 3925,3930; Crosslines 3960,3965,3970) are derived from displacement measurements done in highly deformed, semi-chaotic units near the fault surface, and therefore do not represent true throws.

5.4 Fault 3 reconstruction

Fault 3 reconstruction (Fig. 39) done using the following assumptions:

- The CZ consists of landslide/slump material.
- Horizons *e-g* and *a-d* are characterized by low and high EI values, respectively.
- Maximum displacement represents the fault's growth initiation zone between horizons *d-e*.
- Nucleation is unlikely to occur at the fault's upper part which consists of clay-rich strata characterized by low shear strength (Almagor, 1986; Baudon and Cartwright, 2008a).
- Fault blind nucleation prior to growth is assumed to occur at the *f* horizon.
- Maximum displacement migrated from the point of nucleation (Peacock, 1991).

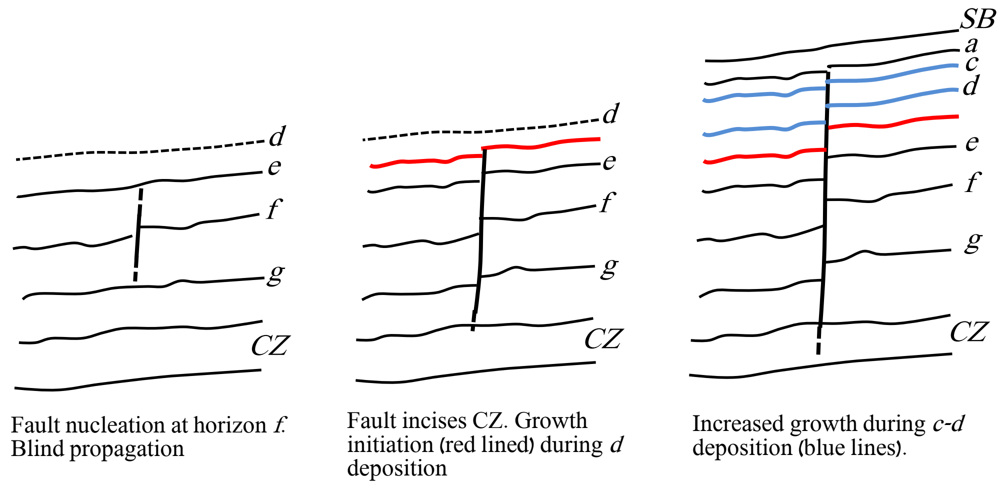

Figure 39. Fault 3 reconstruction.

5.5 Restoration limitations

Dividing key horizons into seismic packages emphasizes the challenges that resolution plays regarding restoration models. This is especially critical where no borehole or geophysical data is available, making the separation of seismic packages full of pitfalls, which directly correlate into restoration models.

Restoration models in this research are based on 7 key horizons while T-Z and DCD plots are based on broader displacement data. Crossline 3990 shows how these differences can result in different interpretations regarding fault evolution (Fig. 38). The detailed 3990 T-Z plot suggests the possibility of a growth phase, implied from the stepped profile initiating at ~500m depth, right under key horizon *d*. According to this plot, maximum displacement accounts for growth initiation. In comparison the 3990b plot, which is based only on key horizons as the restoration models, can be interpreted as representing blind propagation. In addition, maximum displacement is measured at horizon *e*, 80m deeper as compared to 3990, thus suggesting a deeper, blind nucleation point.

Despite these limitations, the restoration model sheds light regarding the growth-related *c-d* package, which can be divided into 2 separate seismic units (Fig. 40): an upper unit characterized by strong continuous reflections; and a lower unit characterized by weak, discontinuous reflections. This could be interpreted as a sedimentary unit overlaying a weak slump unit. This shows how displacement analysis critically depends on the division key horizons as these can lead to changes in both the T-Z plots and restoration models. Still, these will not affect DCD plots, thus emphasizing the importance of using multiple displacement analysis methods.

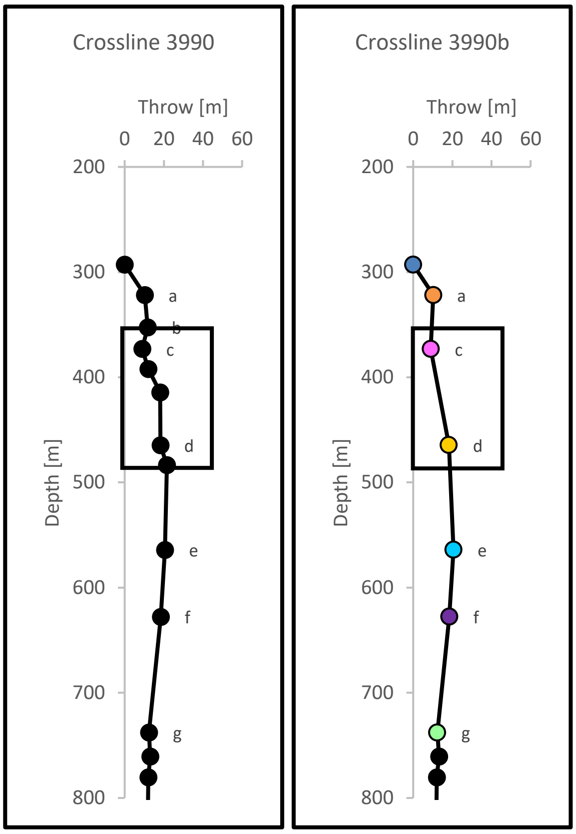

Figure 40. Crossline 3990 T-Z plots interpretations. Left- the original plot, including all measurements also used for DCD plots. Right- T-Z plot limited for key horizons.

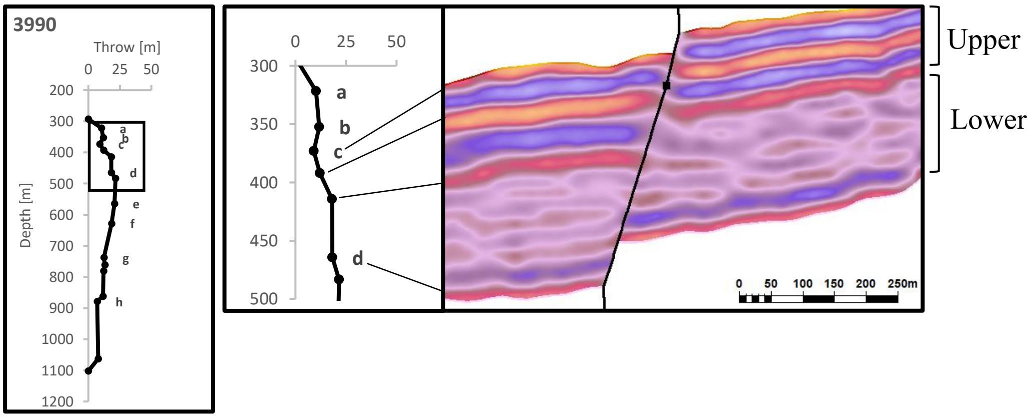

Figure 41. Suggested c-d package interpretation. The abrupt change in reflections suggests the c-d package can be divided into upper and lower packages, resulting in differing displacement analyses.

5.6 Conclusions

- EI calculations, based on detailed T-Z and DCD plots, deliver quantitative evidence for fault evolution. This allows setting EI criteria?on for the growth phase, supported by restoration models.
- Normal faults in the Gabriella survey are restricted by geological structures, manifested by different displacement patterns. Maximum displacement zones suggest all faults nucleated at ~600-700m depth.
- Chaotic structures control fault evolution, recorded as abrupt changes in displacement values resulting in irregular displacement patterns. This, due to their weak mechanical properties, causes them to be less resistant to shear.
- Combining DCDs with well data and sedimentation rates allows one to determine the age of growth phases.

5.7 Summary

This research presents detailed displacement analyses of four neighboring normal faults in the Plio-Pleistocene section offshore Israel. Following structural standard interpretation, key horizons are mapped for fault displacement measurements in the northern part of the "Gabriella" 3D seismic dataset. Detailed fault mapping includs seismic attribute validation, which can also be used for identifying chaotic bodies and their relations to the faults. We present a workflow procedure using existing methods, which underscores different types of faults and the influence of chaotic features on fault evolution.

Displacement measurements are crossploted on T-Z & DCD plots, graphical techniques allowing fault growth models classification and blind, growth and other restricted types of faults were identified. Variations in displacement patterns underscore the control of chaotic features, acting to restrict the growing faults. EI values calculated for seismic packages support the fault classification derived from T-Z and DCD plots. Changes in displacement values of key horizons along the strike of the faults emphasize how the analyzed faults evolved differently. Restoration models support the fault classification.

Combination of T-Z & DCD plots together with EI & restoration models permit a better interpretation of fault evolution. This is especially helpful as the faults have similar dimensions and ranges of throw values, resulting in minor changes not seen in less detailed interpretation of the seismic data. The work shows that in progradational settings, fault analysis using only EI values can produce limited or even misleading results. The workflow developed in this research could also be used for separating different fault systems and for highlighting active segments within faults.

6. References

Back, S., C. Hocker, M. B. Brundiers, P.A Kukla. (2006). Three-dimensional-seismic coherency signature of Niger Delta growth faults: integrating sedimentology and tectonics. *Basin Research* 18.3 (2006): 323-337.

Barnett, J. A. M., Mortimer, J., Rippon, J. H., Walsh, J. J., & Watterson, J. (1987). Displacement Geometry in the Volume Containing a Single Normal Fault. *American Association of Petroleum Geologists Bulletin*, *71*(8), 925–937. http://doi.org/10.1306/948878ED-1704-11D7-8645000102C1865D

Baudon, C., & Cartwright, J. (2008a). Early stage evolution of growth faults: 3D seismic insights from the Levant Basin, Eastern Mediterranean. *Journal of Structural Geology*, *30*(7), 888–898. http://doi.org/10.1016/j.jsg.2008.02.019

Baudon, C., & Cartwright, J. A. (2008b). 3D seismic characterisation of an array of blind normal faults in the Levant Basin, Eastern Mediterranean. *Journal of Structural Geology*, *30*(6), 746–760. http://doi.org/10.1016/j.jsg.2007.12.008

Bertoni, C., & Cartwright, J. A. (2006). Controls on the basinwide architecture of late Miocene (Messinian) evaporites on the Levant margin (Eastern Mediterranean). *Sedimentary Geology*, *188–189*, 93–114. http://doi.org/10.1016/j.sedgeo.2006.03.019

Buchbinder, B., & Zilberman, E. (1997). Sequence stratigraphy of Miocene-Pliocene carbonate-siliciclastic shelf deposits in the eastern Mediterranean margin (Israel): effects of eustasy and tectonics. *Sedimentary Geology*, *112*(1–2), 7–32. http://doi.org/10.1016/S0037-0738(97)00034-1

Cartwright, J. A., and M. P. A. Jackson (2008), Initiation of gravitational collapse of an evaporite basin margin: The Messinian saline giant, Levant Basin, eastern Mediterranean, Geol. Soc. Am. Bull., 120(3-4), 399–413, doi: 10.1130/B26081X.1.

Cartwright, J. A., & Mansfield, C. S. (1998). Lateral displacement variation and lateral tip geometry of normal faults in the Canyonlands National Park, Utah. *Journal of Structural Geology*, *20*(1), 3–19. http://doi.org/10.1016/S0191-8141(97)00079-5

Cartwright, J. A., et al. "Polycyclic motion history of some Gulf Coast growth faults from high-resolution displacement analysis." Geology 26.9 (1998): 819-822.

Catuneanu, O., 2006, Principles of sequence stratigraphy, Elsevier.

Chapman, T. J., & Meneilly, Q. W. (1990). Fault displacement analysis in seismic exploration. *First Break*, *8*(1). http://doi.org/10.3997/1365-2397.1990001

Childs, C., Nicol, A., Walsh, J. J., & Watterson, J. (2002). The growth and propagation of synsedimentary faults. *Journal of Structural Geology*, *25*(4), 633–648. http://doi.org/10.1016/S0191-8141(02)00054-8

Child, C., Holdsworth, R.E., Jackson, C.A.-L., Manzocchi, T., Walsh, J.J. & Yielding, G. (2017).

The Geometry and Growth of Normal Faults. Geological Society Special Publication 439.

Chopra, S., & Marfurt, K. (2007). Seismic curvature attributes for mapping faults/fractures, and other stratigraphic features. *CSEG Recorder*, (November), 38–42.

Cowie, P. A., & Scholz, C. H. (1992). Displacement-length scaling relationship for faults: data synthesis and discussion. *Journal of Structural Geology*, *14*(10), 1149–1156. http://doi.org/10.1016/0191-8141(92)90066-6

Dawers, N. H., & Anders, M. H. (1995). Displacement-length scaling and fault linkage. *Journal of Structural Geology*, *17*(5). http://doi.org/10.1016/0191-8141(94)00091-D

Druckman, Y., Conway, B.H., Eshet, Y., Gill, D., Lipson-Benitah, S., Moshkovitz, S., Perelis Grossowicz, L., Rosenfeld, A., Siman-Tov, R ., 1994. The stratigraphy of the Yam Yafo 1 Borehole. Geol. Surv. Isr., Rep. GSI/28/94,2 7p.

Edwards, M. B. (1995). Differential subsidence and preservation potential of shallow-water Tertiary sequences, northern Gulf Coast Basin, USA. *Sedimentary Facies Analysis; a Tribute to the Research and Teaching of Harold G. Reading.* http://doi.org/10.1002/9781444304091.ch11

Eruteya, O. E., Safadi, M., & Waldmann, N. (2016). Submarine Mass Movements and their Consequences, *41*, 39–47. http://doi.org/10.1007/978-3-319-20979-1

Freund, R. Goldberg., M. Weissbrod, T., Druckman, Y., and Derin, B., 1975. The Triassic-Jurassic Structure of Israel and its relation to the origin of the Eastern Mediterranean: Geogloical Survey of Israel. Bulletin 65, p. 26. ,

Frey-Martinez, J., J. Cartwright, and B. Hall (2005), 3D seismic interpretation of slump complexes: examples from the continental margin of Israel, Basin Res., 17(1), 83–108, doi:10.1111/j.1365-2117.2005.00255.x.

Galloway, W. E. (1986). Growth faults and fault-related structures of prograding terrigenous clastic continental margins, AAPG Bullitin, 70(1), 121–128.

Gardosh, M., Druckman, Y., Buchbinder, B., & Rybakov, M. (2006). The Levant Basin Offshore Israel: Stratigraphy, Structure, Tectonic Evolution and Implications for Hydrocarbon Exploration The Levant Basin Offshore Israel: Stratigraphy, Structure, Tectonic Evolution and Implications for Hydrocarbon Exploratio. *GSI Report*, *14/2006* (December), 119.

Gardosh, M., Y. Druckman, B. Buchbinder, and R. Calvo (2008), The Oligo-Miocene deepwater system of the Levant Basin. Geological Survey of Israel.

Garfunkel, Z., and G. Almagor. "Active salt dome development in the Levant Basin, southeast Mediterranean." Dynamical geology of salt and related structures. 1987. 263-300.

Gvirtzman, G. and Buchbinder, B., 1978. The Tertiary history of the coastal plain and continental shelf of Israel and its bearing on the history of the Eastern Mediterranean. Initial Report Deep Sea Drilling Project, 42B, 1195-1222

Gradmann, S., C. Hübscher, Z. Ben-Avraham, D. Gajewski, and G. Netzeband (2005), Salt tectonics off northern Israel, Mar. Pet. Geol., 22(5), 597-611, doi:10.1016/j.marpetgeo.2005.02.001.

Hensen F.R.S., 1951. Observationson the geology of the petroleum occurrences of the Middle East, in 3rd World Pteroleum Congress: The Hauge, The Netherlands, World Petroleum Congress, p. 118-140.

Herron. D.A. (2011). First steps in seismic interpretation. SEG Books, Geophysical Monograph Series No. 16, 203 p.

Lang, G. (2016). 3D seismic stratigraphy of the Plio-Pleistocene section of the Levant continental margin- reconstructing continental margin development in light of tectonic, sedimentary and eustatic processes. Haifa University

Mansfield, C. S., & Cartwright, J. a. (1996). High resolution fault displacement mapping from three-dimensional seismic data: evidence for dip linkage during fault growth. *Journal of Structural Geology*, *18*(2–3), 249–263. http://doi.org/10.1016/S0191-8141(96)80048-4

Muraoka, H., & Kamata, H. (1983). Displacement distribution along minor fault traces. *Journal of Structural Geology*, *5*(5), 483–495. http://doi.org/10.1016/0191-8141(83)90054-8

Ngeri, A.P., Tamunobereton-ari, I., and Amakiri A.R.C. (2015). Ant-Tracker Attributes: An Effective Approach To Enhancing Fault Identification And Interpretation. *IOSR Journal of VLSI and Signal Processing (IOSR-JVSP)* Volume 5, Issue 6, Ver. II (Nov -Dec. 2015), PP 67-73. DOI: 10.9790/4200-05626773

Nicol, A., Watterson, J., Walsh, J. J., & Childs, C. (1996). The shapes, major axis orientations and displacement patterns of fault surfaces. *Journal of Structural Geology*, *18*(2–3), 235–248. http://doi.org/10.1016/S0191-8141(96)80047-2

Paldor, E. (2016). Disturbence events since the later Neogene: Evidence from the subsurface (shallow seismics). The Hebrew University of Jerusalem

Petersen, K., Clausen, O. R., & Korstgård, J. A. (1992). Evolution of a salt-related listric growth fault near the d-1 well, block 5605, Danish North Sea: displacement history and salt kinematics. *Journal of Structural Geology*, *14*(5), 565–577. http://doi.org/10.1016/0191-8141(92)90157-R

Rippon, J. H. (1985). Contoured patterns of the throw and hade of normal faults in the Coal Measures (Westphalian) of north-east Derbyshire. *Proceedings of the Yorkshire Geological Society*, *45*(3), 147–161. http://doi.org/10.1144/pygs.45.3.147

Safadi, M., Meilijson, A., Makovsky, Y. (2017) Internal deformation of the southeast Levant margin through continued activity of buried mass transport deposits. *Tectonics* Http://doi.org/10.0002/2016TC004342

Schlische, R. W., & Anders, M. H. (1996). Stratigraphic effects and tectonic implications of the growth of normal faults and extensional basins. *History of Basin and Range Extension Using Sedimentology and Stratigraphy, Geological Society of America Special Paper*, *303*, 183–203. http://doi.org/10.1130/0-8137-2303-5.183

Sivan,D.,Gvirtzman,G.&Sass,E. (1999) Quaternary stratigraphy and paleogeography of the Galilee coastal plain, Israel. Quat. Res.,51 , 280-294.

Thorsen, C.E. (1963). Age of growth faulting in the southeast Louisiana. GCAGS Tansactions. Vol. 13, pages 103-110

Tibor, G., & Ben-Avraham, Z. (1992). Late Tertiary seismic facies and structures of the Levant passive margin off central Israel, eastern Mediterranean. *Marine Geology*, *105*(1–4), 253–273. http://doi.org/10.1016/0025-3227(92)90192-K

Veeken, P.C.H., & Moerkerken (2013). Seismic stratigraphy and depositional facias models. EAGE

Walsh, J. J., & Watterson, J. (1989). Displacement gradients on fault surfaces. *Journal of Structural Geology*, *11*(3), 307–316. http://doi.org/10.1016/0191-8141(89)90070-9

Watterson, J. (1986). Fault dimensions, displacements and growth. *Pure and Applied Geophysics PAGEOPH*, *124*(1–2), 365–373. http://doi.org/10.1007/BF00875732

Yilmaz, O. (2010). Seismic Data Analysis. Vol 2. SEG.

7. Appendix

Appendix 1.

Fault 1 T-Z plots.

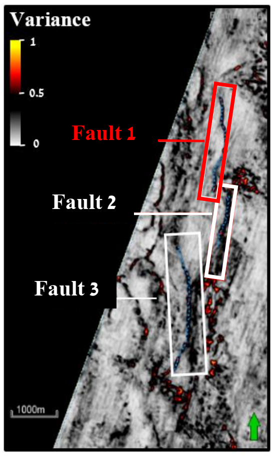

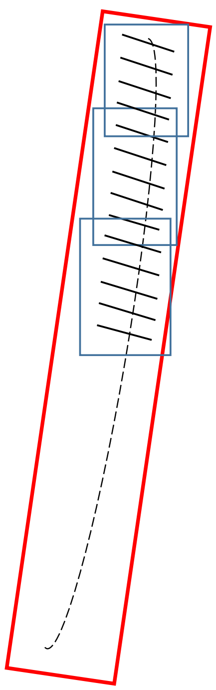

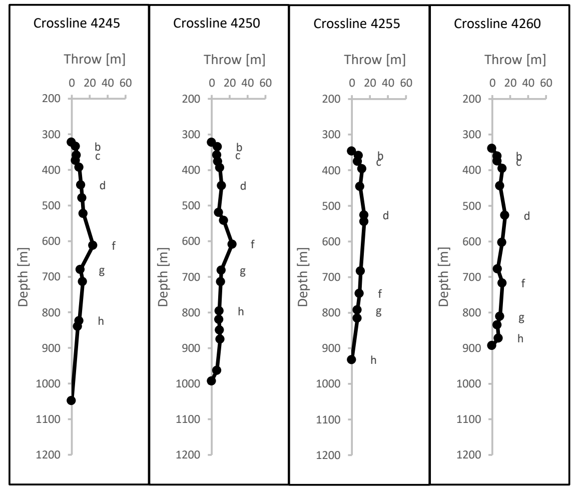

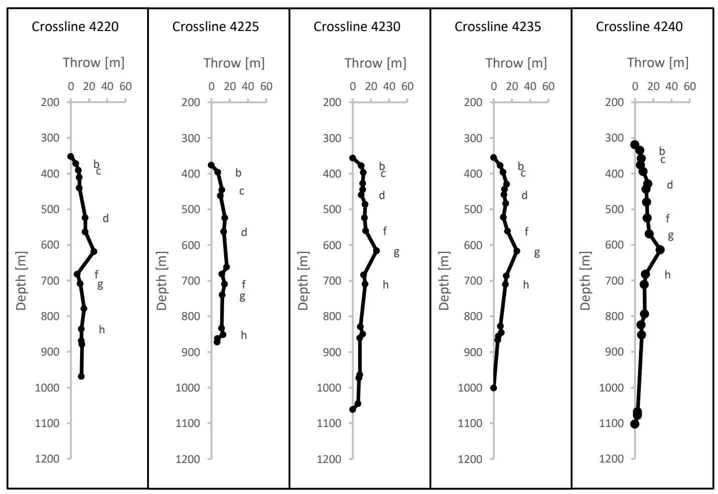

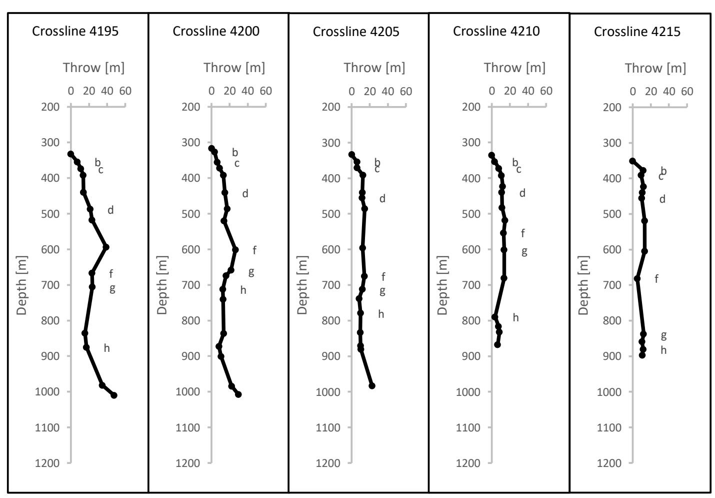

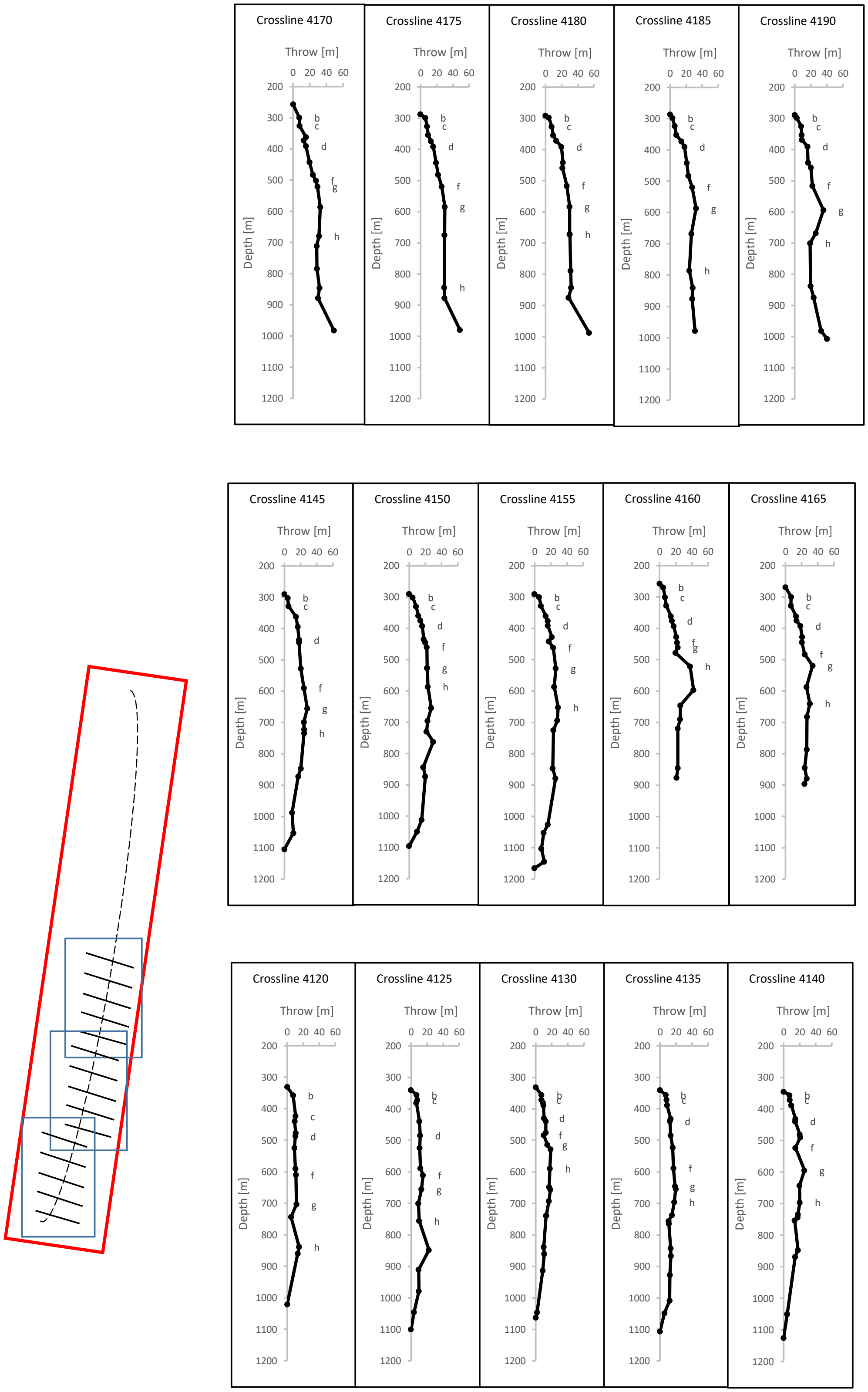
Crossline 4170
Crossline 4175
Crossline 4180
Crossline 4185
Crossline 4190
Crossline 4145
Crossline 4150
Crossline 4155
Crossline 4160
Crossline 4165
Crossline 4120
Crossline 4125
Crossline 4130
Crossline 4135
Crossline 4140
Throw [m]
Depth [m]

Appendix 2.

Fault 2 T-Z plots.

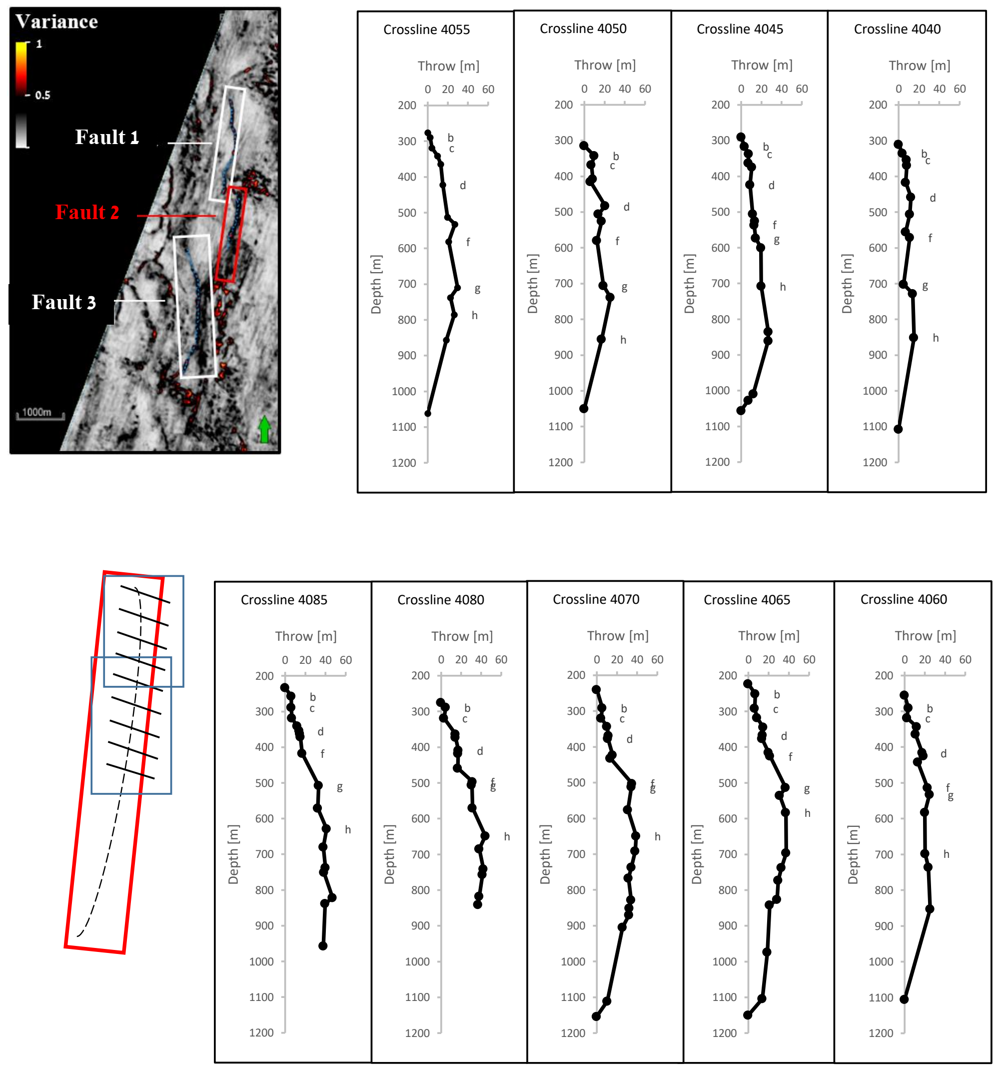

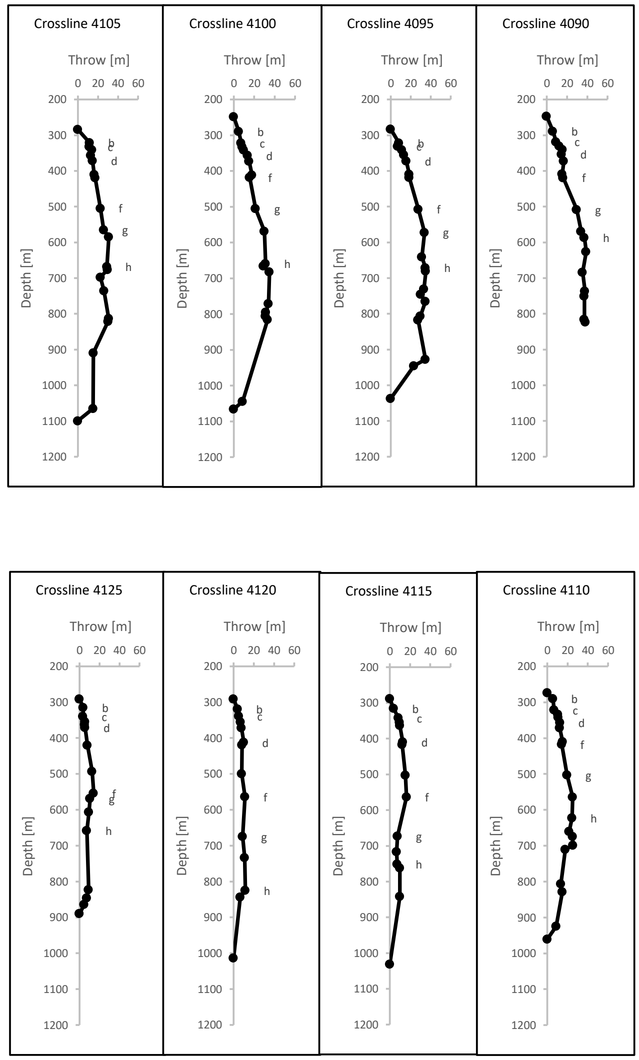
Crossline 4105
Crossline 4100
Crossline 4095
Crossline 4090
Crossline 4125
Crossline 4120
Crossline 4115
Crossline 4110
Throw [m]
Depth [m]

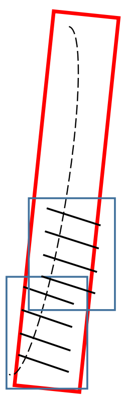

Appendix 3.

Fault 3 T-Z plots.

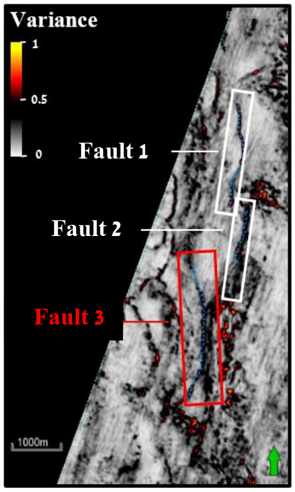

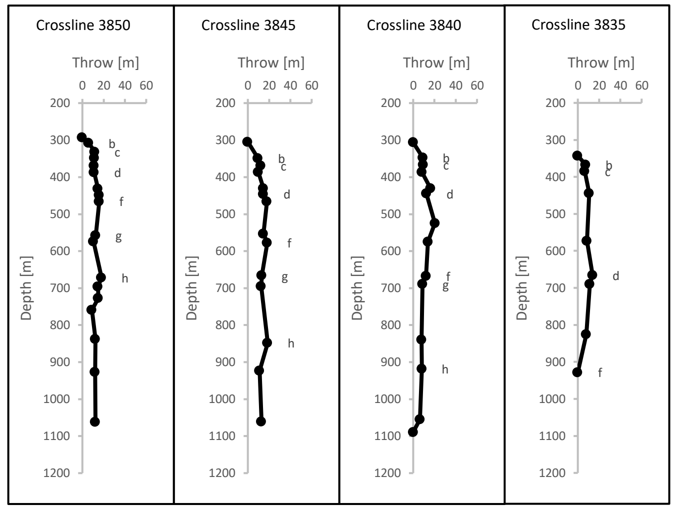

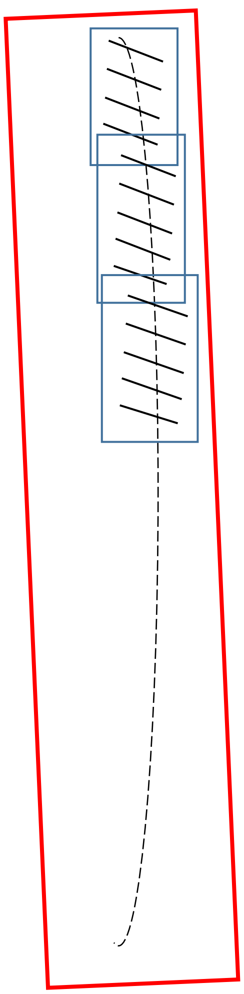

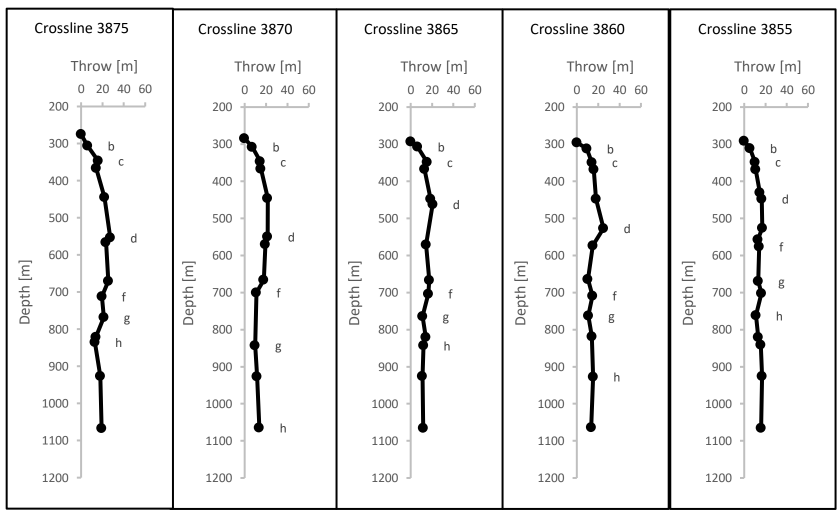

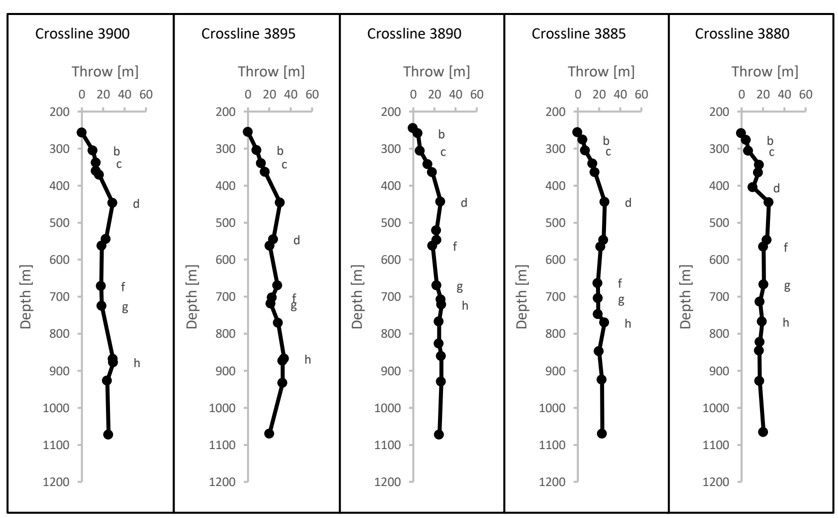

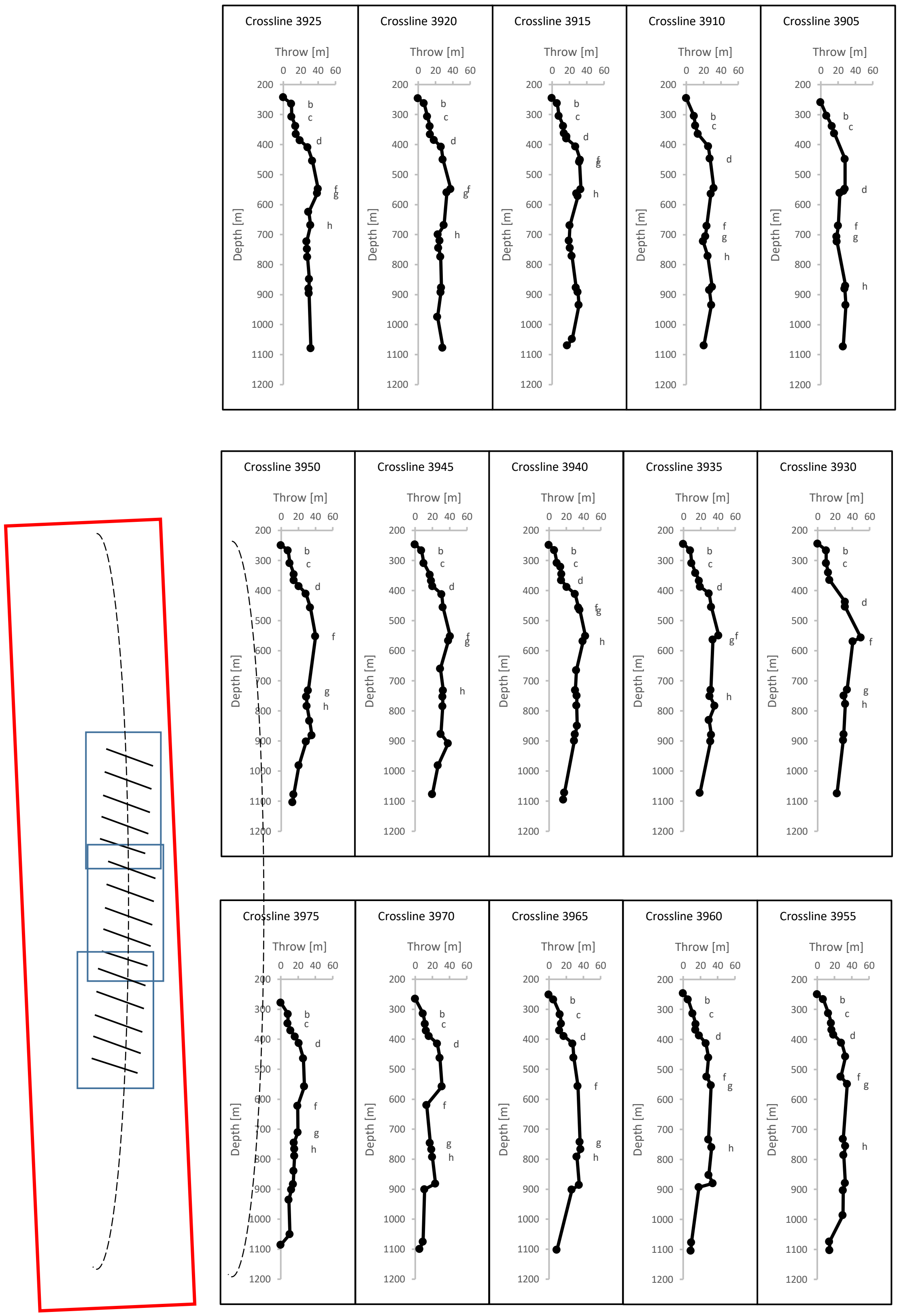
Crossline 3925
Crossline 3920
Crossline 3915
Crossline 3910
Crossline 3905
Crossline 3950
Crossline 3945
Crossline 3940
Crossline 3935
Crossline 3930
Crossline 3975
Crossline 3970
Crossline 3965
Crossline 3960
Crossline 3955
Throw [m]
0 20 40 60
Depth [m]
200
300
400
500
600
700
800
900
1000
1100
1200
b
c
d
f
g
h

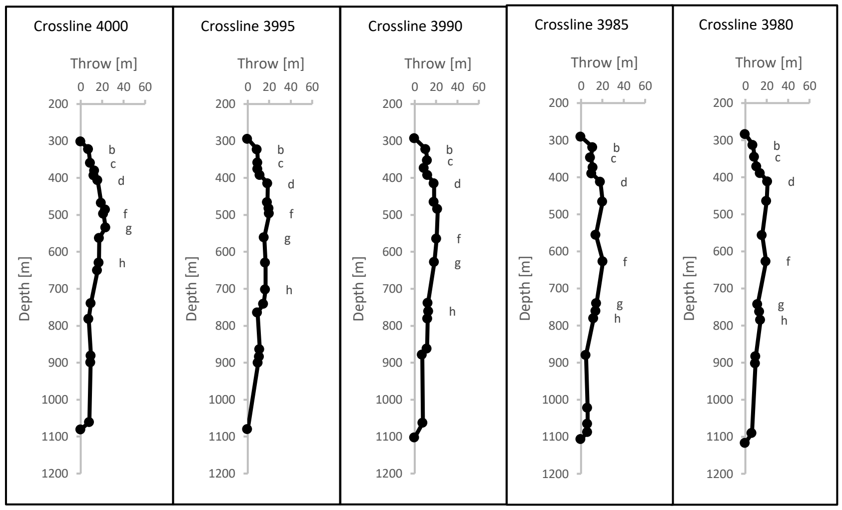
Crossline 4000
Crossline 3995
Crossline 3990
Crossline 3985
Crossline 3980
Throw [m]
Depth [m]

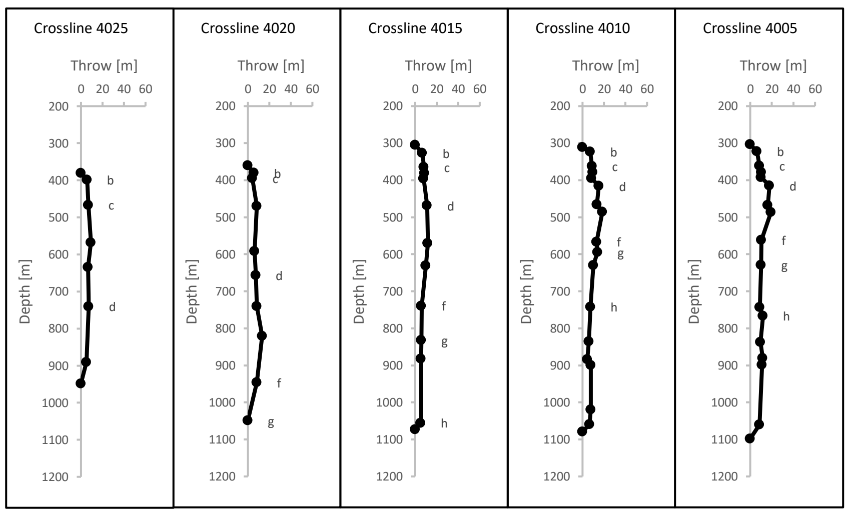
Crossline 4025
Crossline 4020
Crossline 4015
Crossline 4010
Crossline 4005
Throw [m]
Depth [m]

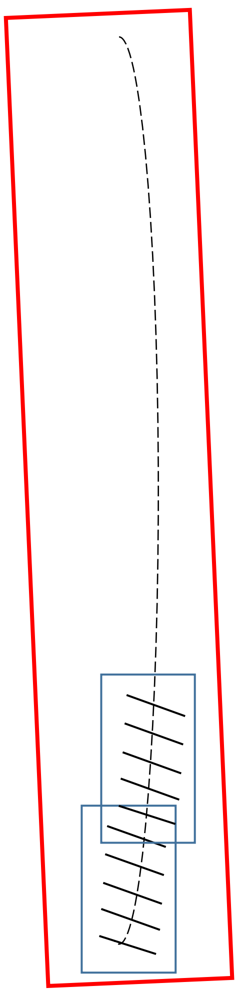

Appendix 4.

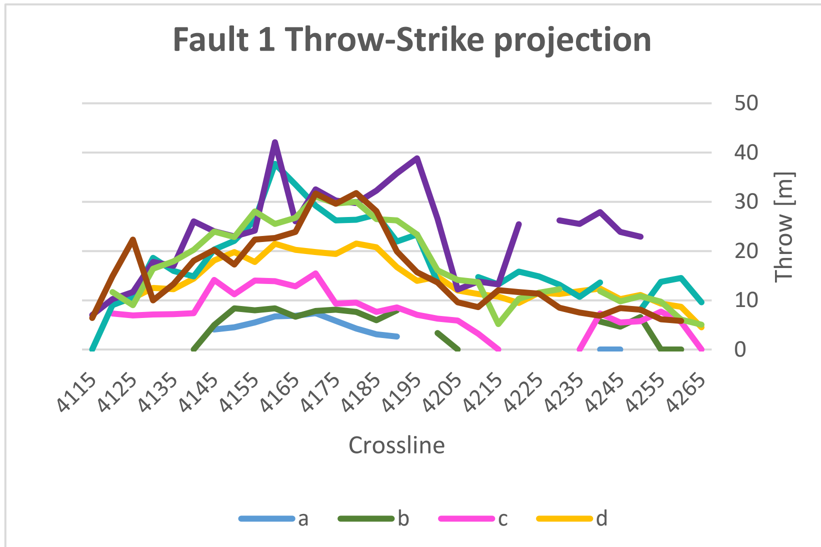

Appendix 5.

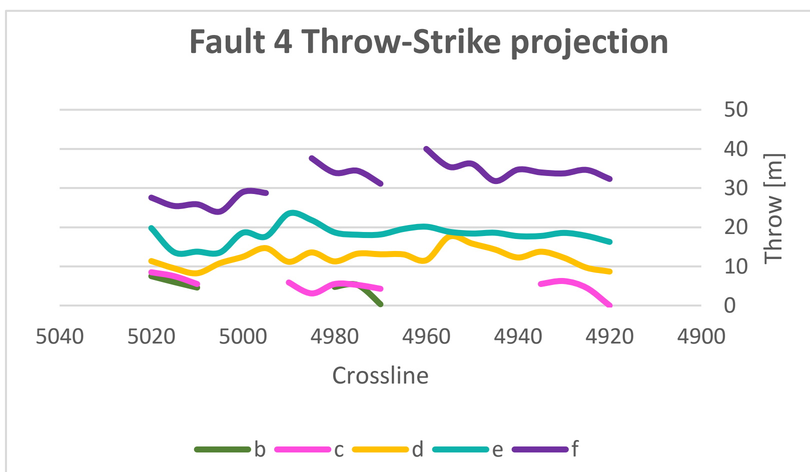

תקציר

החתך הפליו-פלייסטוקני במדף היבשת מול חופי ישראל מאופיין במספר רב של גלישות קרקע, ביניהן גלישה רחבת היקף בשם ה-Israel Slump Complex (ISC). גלישות אלו נחצות ע״י מערכות העתקה המאופיינות בהעתקים נורמלים מסוג thin-skinned. המחקר בוחן את השפעת גלישות הקרקע על התפתחות ההעתקים החוצים אותן, דרך ניתוח כמותי של מדידות הסטה (displacements) על גבי משטחי ההעתקים.

באמצעות פענוח סייסמי מופו מספר גלישות קרקע ומערכות העתקה ברישיון גבריאלה, סקר סייסמי תלת-מימדי ברזולוציה גבוהה בממד העומק, הממוקם כ-12 ק״מ מול חופי נתניה. החתך הסטרטיגרפי בנפח כולל את חבורות סקיה וכורכר, כאשר חלקו התחתון תחום ע״י תצורת מבקיעים האוופוריטית. מערכות ההעתקים בחתך מאופיינות בהעתקים בלתי מוגבלים (blind) והעתקי גדילה. עם זאתף השקעה פרוגרדטיבית במהלך הפלייסטוקן המאוחר הופכת לאתגר את סיווג ההעתקים.

שיטת העבודה כללה מיפוי נרחב של 10 אופקי מפתח למדידת השתנות גודל ההסטה על גבי משטחי ההעתקים. ניתוח המדידות נעשה בשימוש דיאגרמות הסטה מול עומק (T-Z plots), דיאגרמות קווים שווי-הסטה (Displacement contour diagrams) ומדידת גרדיאנטי הסטה. שלבי הגדילה בהתפתחות ההעתקים, התבטאים בהתעבות החתך הליתולוגי, זוהו בעזרת אינדקסי התרחבות (Expansion indices). שילוב של שיטות אלה איפשר להבחין בין מודלים שונים של התפתחות ההעתקים, וסייע למיפויים במדויק. שינויים בתבניות ההסטה מדגישים כיצד גלישות הקרקע פועלות כגורם מגביל על ההתפתחות ההעתקים.

שתי מערכות העתקה זוהו: מערכת העתקה צפונית (NFZ) המאופיינת בהעתקים נומרלים סינתטיים שכיוונם העיקרים צפ׳-דר׳, ומערכת העתקה דרומית (SFZ) המאופיינת בהעתקים נורמלים סינתטיים ואנתיטיים בכיוון צפ׳-מע׳ – דר׳-מז׳. פענוח מפורט של ארבעה העתקים הראה סוגי התפתחות שונים: (1) העתק בלתי מוגבל (blind); (2) העתק גדילה שהתפתח תחילה כהעתק בלתי מוגבל, כאשר המעבר לשלב הגדילה עקב חצייתו דרך ה-ISC תוארך ל – 0.5-0.71 מ״ש; (3) העתק מוגבל עם שני אזורי הסטה מקסימליים, עקב חצייה של חלקו המרכזי-תחתון דרך מבנה גלישה קטן; (4) העתק מוגבל בתחתית המאופיין בגרדיאנטי הסטה גדולים וסגירה מהירה בחלקו התחתון.

העבודה מדגימה כיצד גלישות קרקע מעודדות פעילות העתקה, היכולה לבוא לידי ביטוי הן בהפעלת מקטע מסויים בתוך ההעתק והן בהפעלה לכל אורכו, כאשר התלות נקבעת ביחס המרחבי בין הגלישה להעתק החוצה אותה. המחקר מציג תוצאות אמפיריות המאפשרות להפריד בין שלבי ההתפתחות השונים של ההעתק: שלב התפתחות בלתי מוגבלת ושלב התפתחות גדילה. תזרים העבודה שפותח בעבודה זו יכול לסייע במציאת אזורים בעלי סיכון מוגבר להפעלת העתקים.

THE HEBREW UNIVERSITY OF JERUSALEM

החוג לגיאולוגיה

המכון למדעי כדור הארץ

הפקולטה למתמטיקה ומדעי הטבע

האוניברסיטה העברית בירושלים

התפתחות העתקים נורמלים: תבניות הסטה בסייסמיקה תלת מימדית ממזרח אגן הלבנט

עבודת גמר לתואר מוסמך במדעי הטבע

מוגשת על ידי:

נדב נבון

בהדרכת:

פרופ' אמוץ עגנון

ד"ר בנימין מדבדב

ספטמבר 2018

אלול תשע"ח